



Supplement of

Very early identification of a bimodal frictional behavior during the post-seismic phase of the 2015 M_w 8.3 Illapel, Chile, earthquake

Cedric Twardzik et al.

Correspondence to: Cedric Twardzik (twardzik@unistra.fr)

The copyright of individual parts of the supplement might differ from the article licence.

Contents

	S1 Estimated static offsets for the two largest aftershocks and the mainshock	2
	S2 Post-processing of the kinematic position time series	5
	S3 Choice of the smoothing parameter	13
5	S4 Summary of the results from the inversions.	14
	S5 Sensitivity analysis	24
	S6 Comparison between the post-seismic slip model and various co-seismic slip models	29
	S7 Comparison between very early post-seismic slip and very early aftershocks using Frank et al. (2017) catalog	33

S1 Estimated static offsets for the two largest aftershocks and the mainshock

Table 1. Static offsets inferred from the 30-seconds position time series for the M_w 7.1 aftershock. See Figure 1 in the main text for the location of each station. We also show the theoretical duration over which the offset is smoothed because of the Kalman filter.

Station name	North (mm)	East (mm)	T_{kalman} (s)
LSCH	0.06 ± 3.09	0.09 ± 2.98	30.0
JUNT	0.01 ± 3.22	-0.35 ± 3.34	30.0
CRZL	0.08 ± 2.92	-0.10 ± 2.65	30.0
RCSD	-0.32 ± 3.21	0.36 ± 2.78	30.0
CERN	3.38 ± 3.50	0.51 ± 3.43	90.0
SANT	0.33 ± 2.85	0.01 ± 2.93	30.0
PEDR	1.00 ± 3.48	-4.53 ± 2.72	120.0
PFRJ	0.34 ± 3.00	0.24 ± 2.63	30.0
LVIL	23.71 ± 3.98	-22.02 ± 3.06	510.0
TOLO	0.52 ± 3.10	-0.88 ± 2.45	30.0
CMBA	-6.95 ± 3.15	-8.67 ± 2.76	240.0
OVLL	0.63 ± 3.45	0.30 ± 3.38	60.0
SLMC	8.28 ± 3.29	-24.55 ± 3.03	450.0
CNBA	-12.79 ± 3.05	-18.23 ± 2.75	360.0
VALL	0.02 ± 3.16	0.06 ± 3.06	30.0

Table 2. Static offsets inferred from the 30-seconds position time series for the M_w 6.8 aftershock. See Figure 1 in the main text for the location of each station. We also show the theoretical duration over which the offset is smoothed because of the Kalman filter.

Station name	North (mm)	East (mm)	T_{kalman} (s)
LSCH	0.02 ± 3.09	-0.09 ± 2.98	30.0
JUNT	0.03 ± 3.22	-0.04 ± 3.34	30.0
CRZL	0.16 ± 2.92	0.40 ± 2.65	30.0
RCSD	-0.06 ± 3.21	0.34 ± 2.78	30.0
CERN	-0.22 ± 3.50	-0.17 ± 3.43	30.0
SANT	0.16 ± 2.85	-0.07 ± 2.93	30.0
PEDR	0.02 ± 3.48	-0.31 ± 2.72	30.0
PFRJ	0.01 ± 3.00	0.30 ± 2.63	30.0
LVIL	-0.24 ± 3.98	-1.99 ± 3.06	90.0
TOLO	-0.04 ± 3.10	0.19 ± 2.45	30.0
CMBA	-2.03 ± 3.15	-3.17 ± 2.76	90.0
OVLL	-0.32 ± 3.45	-0.10 ± 3.38	30.0
SLMC	-0.77 ± 3.29	-1.27 ± 3.03	120.0
CNBA	-5.67 ± 3.05	-6.93 ± 2.75	150.0
VALL	0.16 ± 3.16	-0.41 ± 3.06	30.0

Table 3. Static offsets inferred from the 30-seconds position time series for the M_w 8.3 mainshock. See Figure 1 in the main text for the location of each station. These offsets are used to obtain the co-seismic slip model shown in Supplementary Materials S6. As the position time series are cut at the time of the mainshock (see Twardzik et al. (2019) for more details), there is no smoothing from the Kalman filter. The static offsets are simply computed from the last pre-mainshock position (30 seconds before the origin time) and the first post-mainshock position (5 minutes after the origin time).

Station name	North (mm)	East (mm)
LSCH	-93.52 ± 3.09	-162.56 ± 2.98
JUNT	-59.21 ± 3.22	-106.64 ± 3.34
CRZL	-15.49 ± 2.92	-19.42 ± 2.65
RCSD	3.65 ± 3.21	-0.65 ± 2.78
CERN	39.94 ± 3.50	-56.51 ± 3.43
SANT	18.52 ± 2.85	-23.12 ± 2.93
PEDR	-94.52 ± 3.48	-516.74 ± 2.72
PFRJ	-251.96 ± 3.00	-1389.06 ± 2.63
LVIL	33.18 ± 3.98	-348.64 ± 3.06
TOLO	-112.84 ± 3.10	-240.54 ± 2.45
CMBA	13.16 ± 3.15	-822.50 ± 2.76
OVLL	-222.32 ± 3.45	-699.56 ± 3.38
SLMC	112.80 ± 3.29	-348.84 ± 3.03
CNBA	-6.87 ± 3.05	-1195.47 ± 2.75
VALL	0.45 ± 3.16	-17.11 ± 3.06

10 S2 Post-processing of the kinematic position time series

The following figures (Figure S2.1 to S2.15) show the processing steps to obtain the hourly position time series used in this study. For each station, we show on the top row the raw position time series. The red dashed line indicates the time of the mainshock and the blue dashed lines the time of the two largest aftershock (see main text). The mean and a linear trend have been removed using the 6 days prior to the mainshock origin time. The static offset of the mainshock is also removed. The root mean square (rms) of the time series is calculated using the 6 days prior to the mainshock. The second row shows the position time series after we apply a sidereal filter that is constructed as proposed by Twardzik et al. (2019). This allows the noise level to decrease by $\sim 35\%$ on average. The third row shows the hourly position time series used to obtain the post-seismic slip distribution over the first 12 hours (orange dots). Each position is obtained by computing the average position over a 1-hour long time window that is centered on the time of interest and that spans 30 minutes on either side. Finally, we show on the bottom row the hourly position time series after the 2 largest aftershocks are removed from the raw position time series. The figures are sorted from the northern to the southern stations.

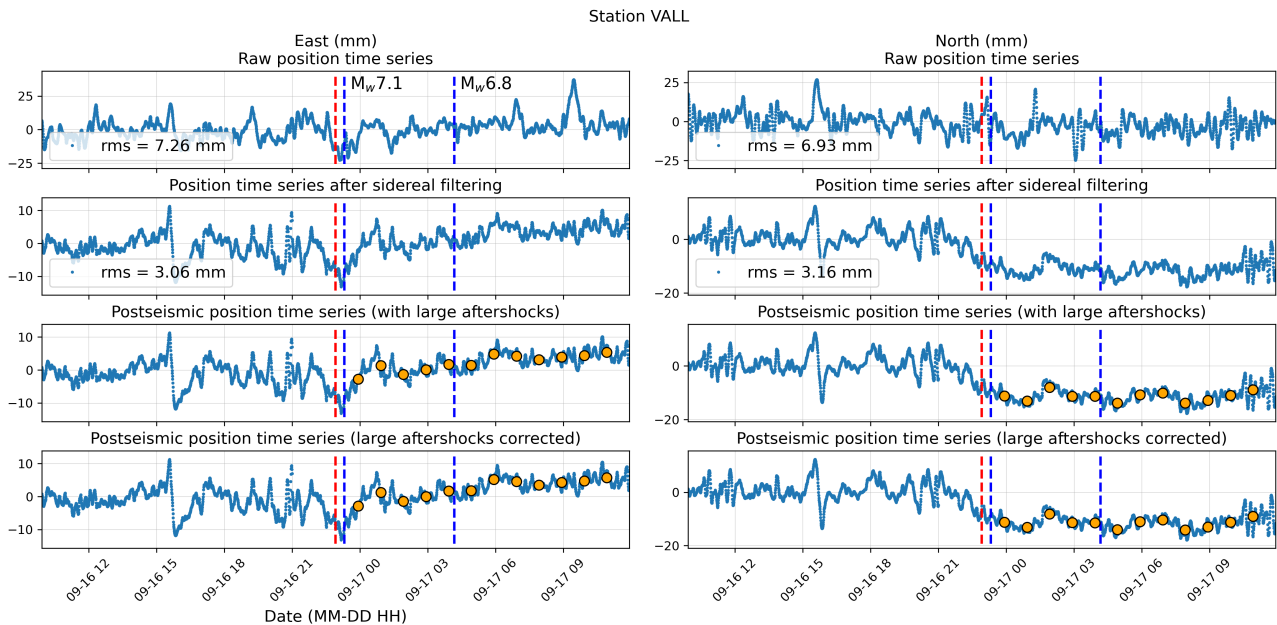


Figure S2.1. Same as Figure 2 in the main text.

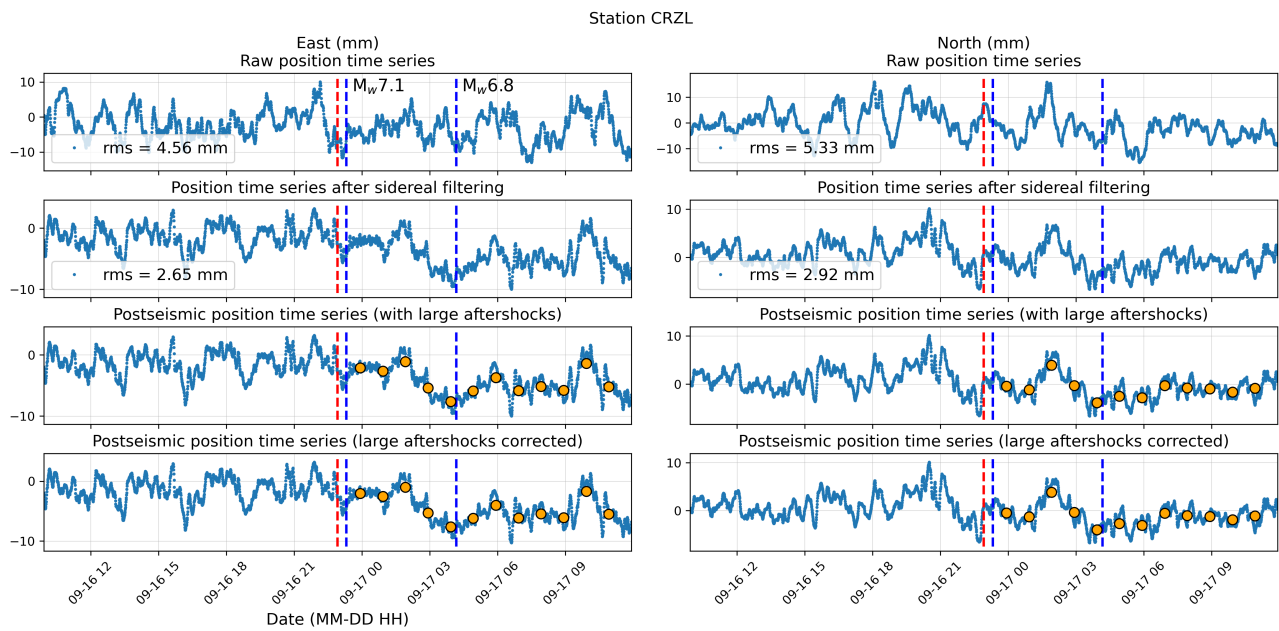


Figure S2.2. Same as Figure 2 in the main text.

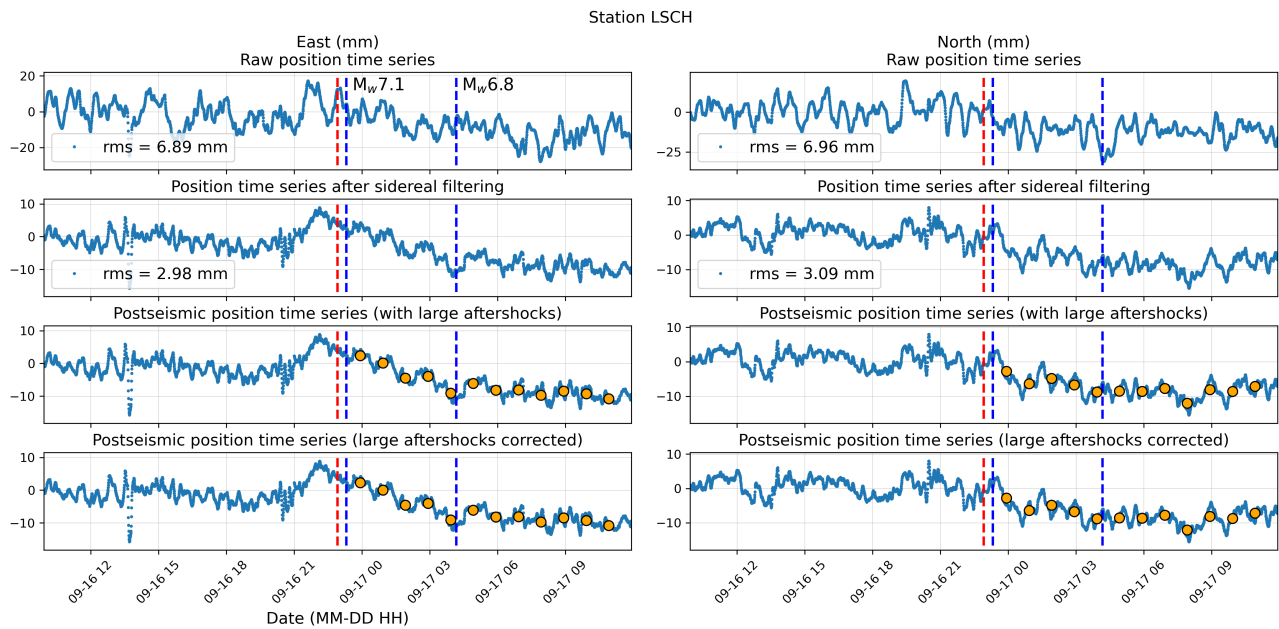


Figure S2.3. Same as Figure 2 in the main text.

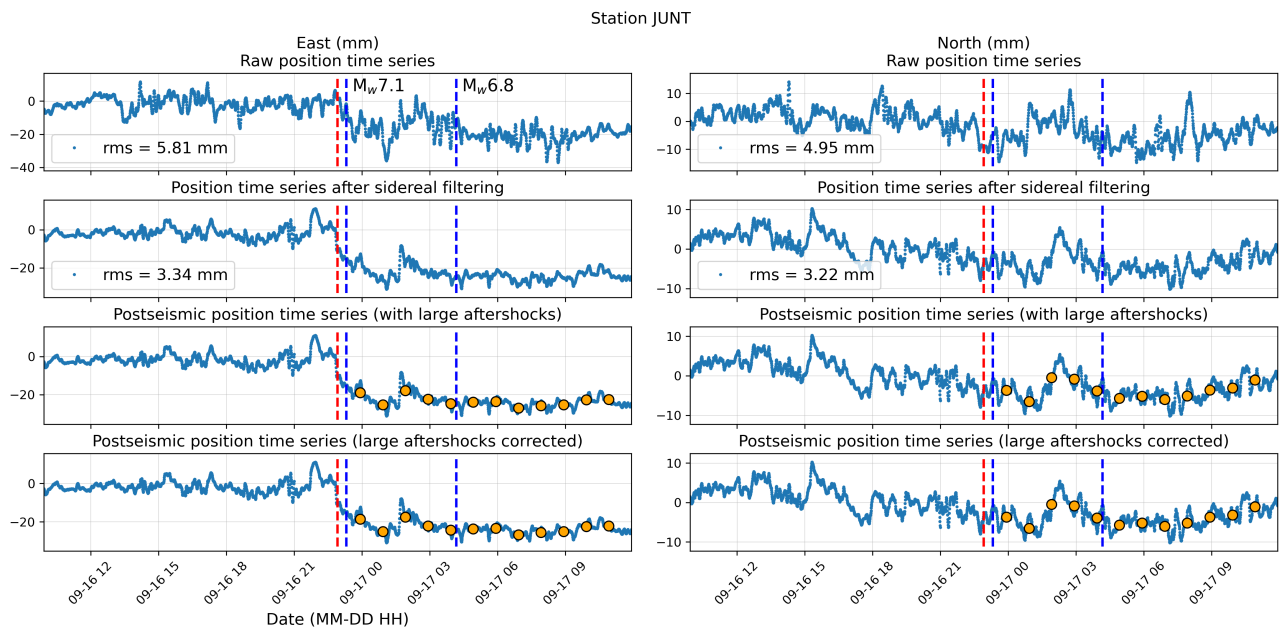


Figure S2.4. Same as Figure 2 in the main text.

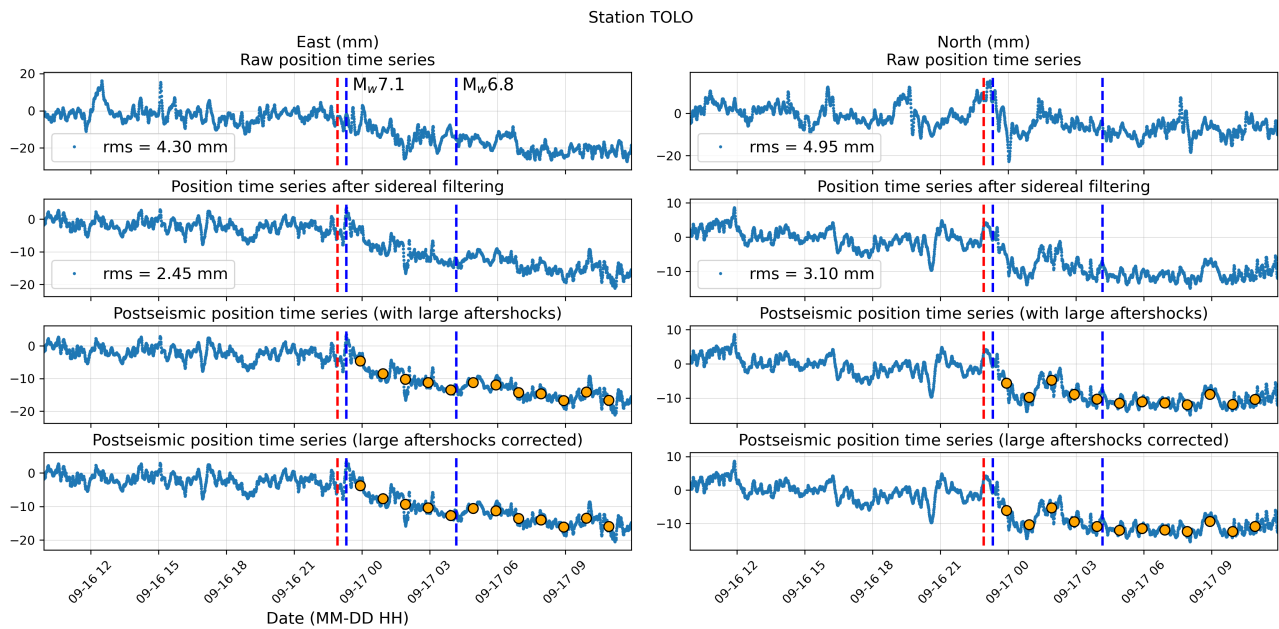


Figure S2.5. Same as Figure 2 in the main text.

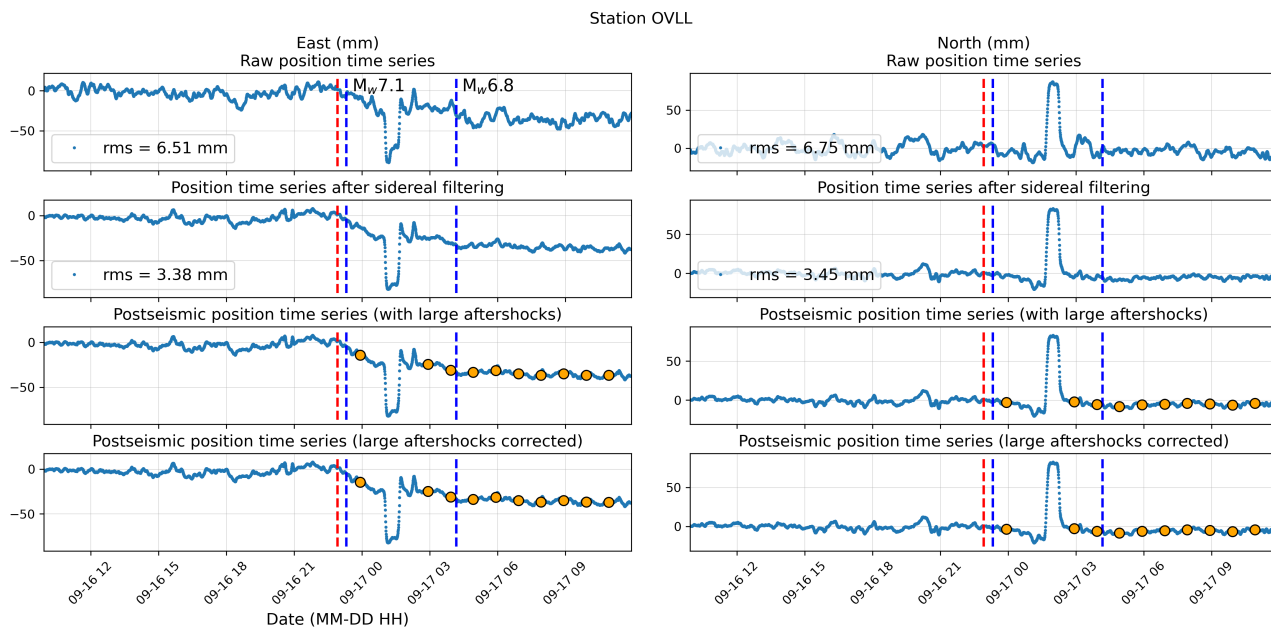


Figure S2.6. Same as Figure 2 in the main text.

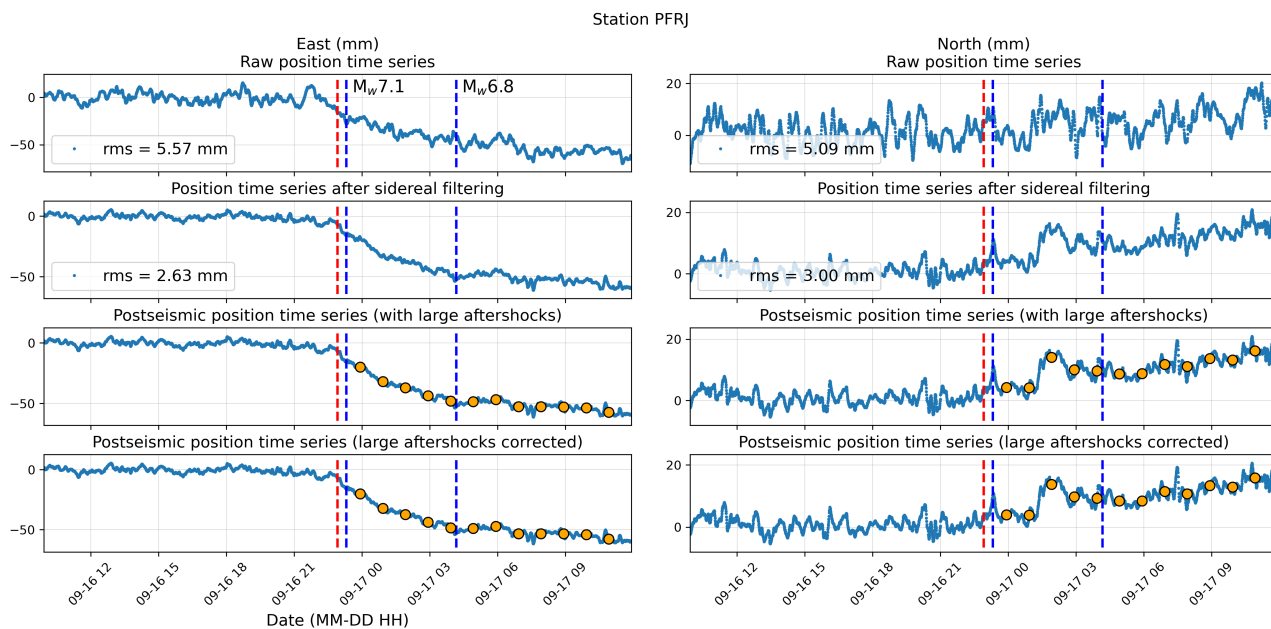


Figure S2.7. Same as Figure 2 in the main text.

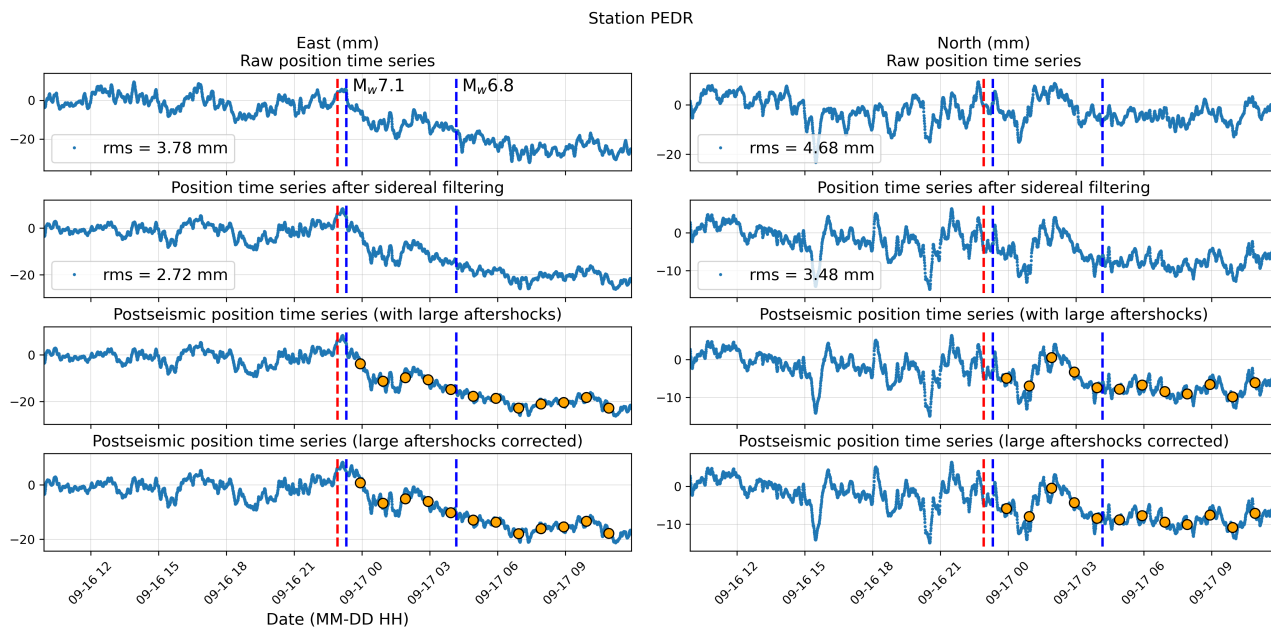


Figure S2.8. Same as Figure 2 in the main text.

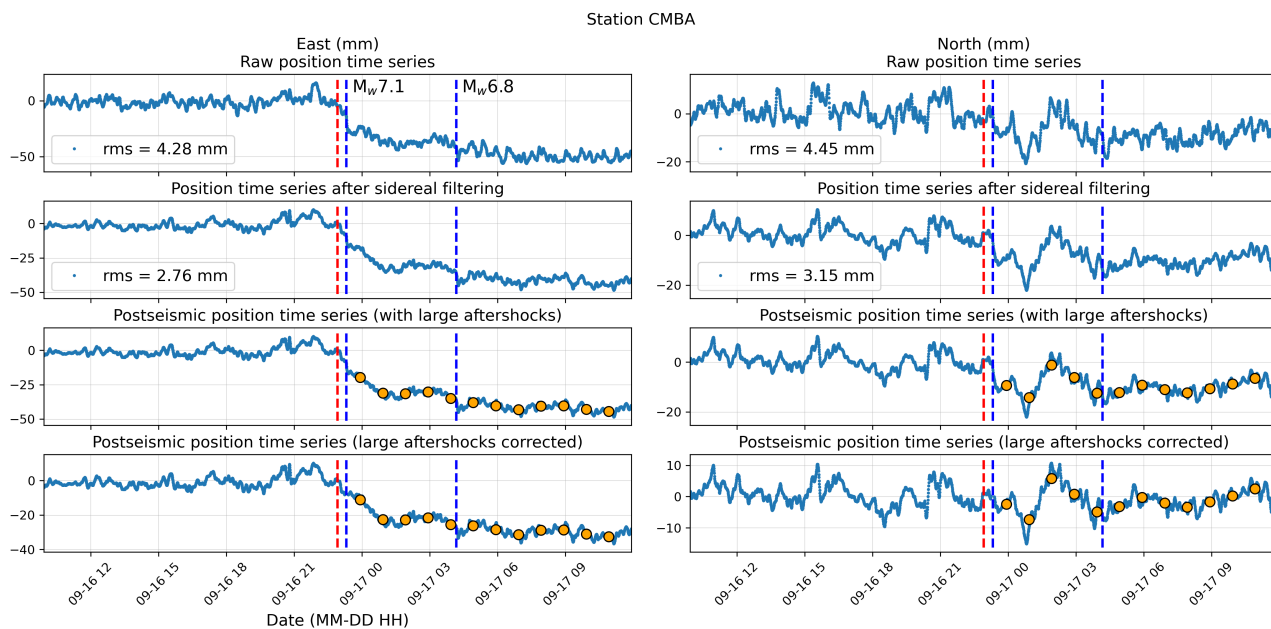


Figure S2.9. Same as Figure 2 in the main text.

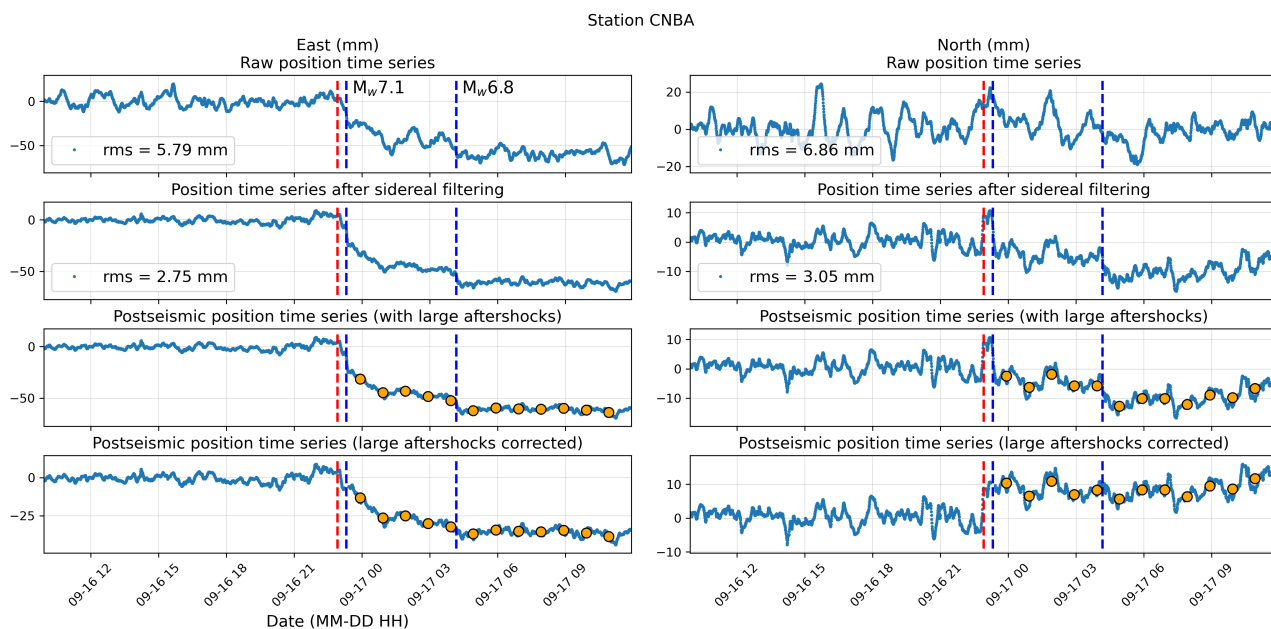


Figure S2.10. Same as Figure 2 in the main text.

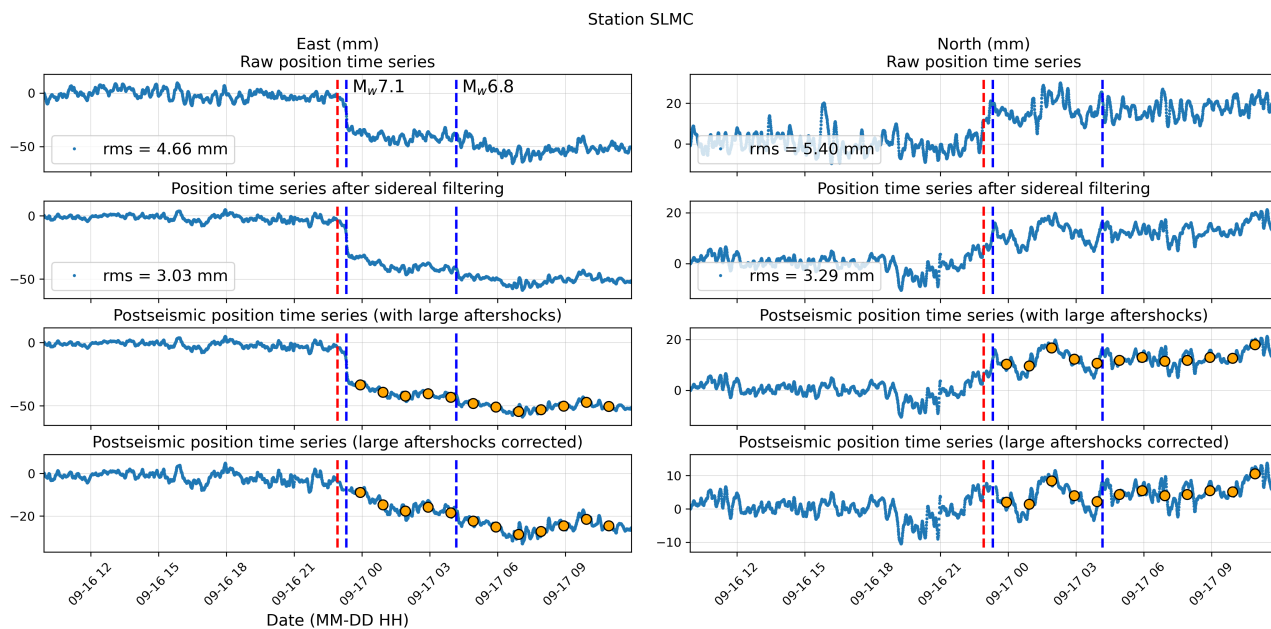


Figure S2.11. Same as Figure 2 in the main text.

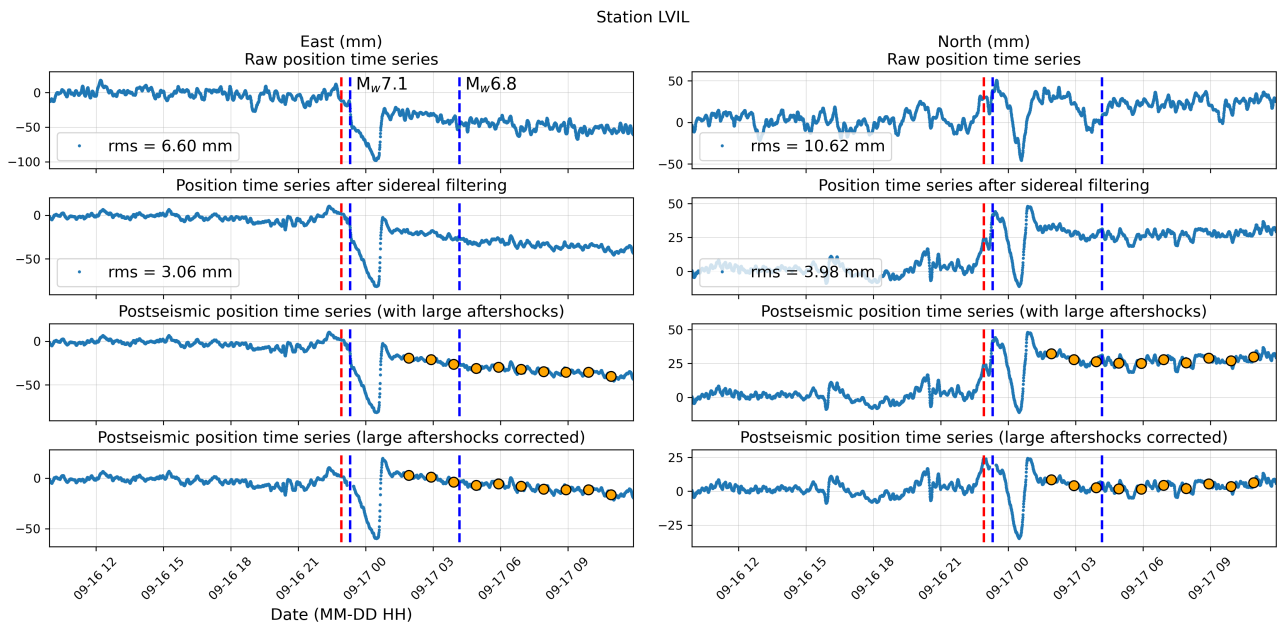


Figure S2.12. Same as Figure 2 in the main text.

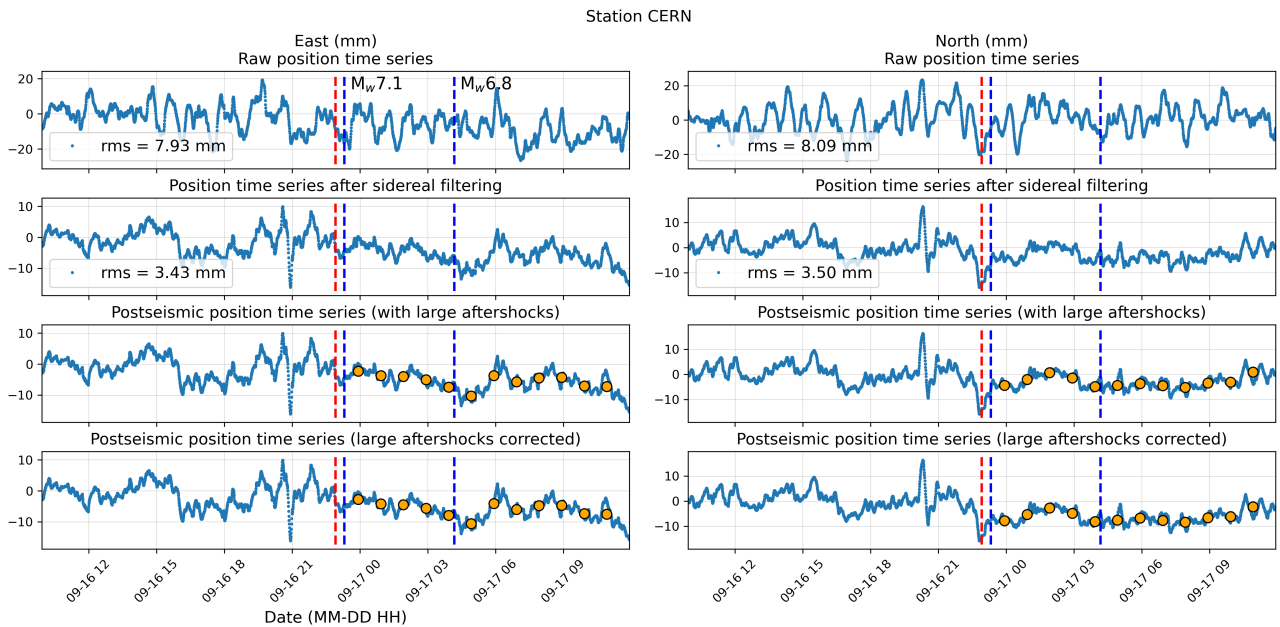


Figure S2.13. Same as Figure 2 in the main text.

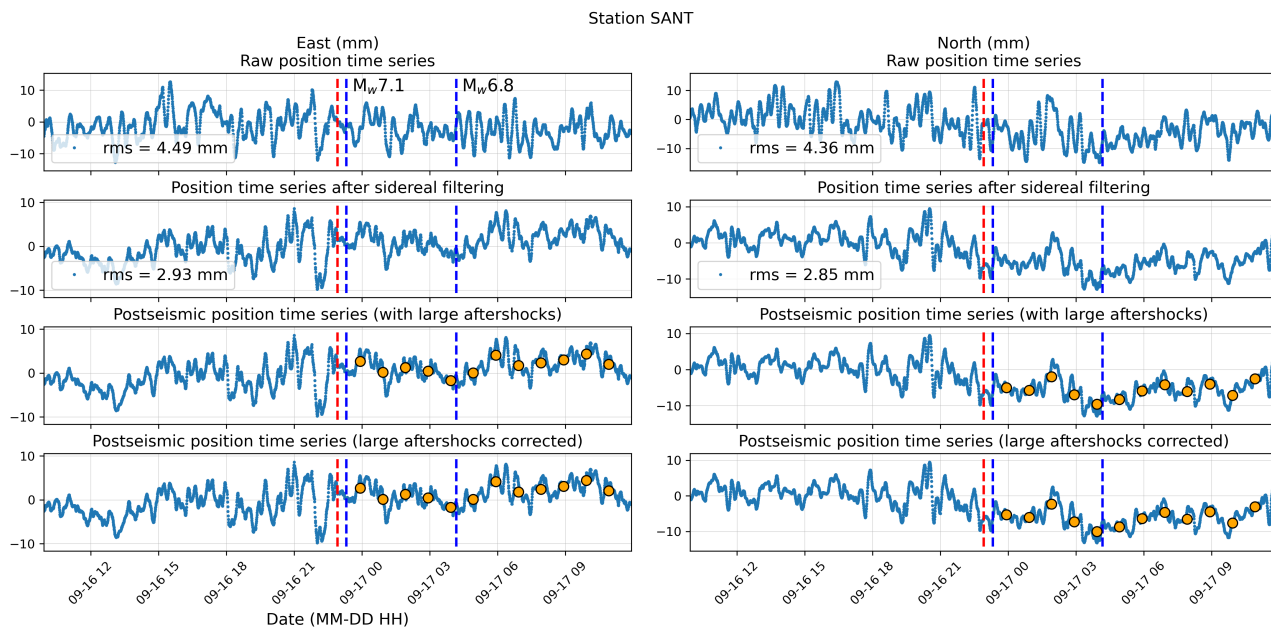


Figure S2.14. Same as Figure 2 in the main text.

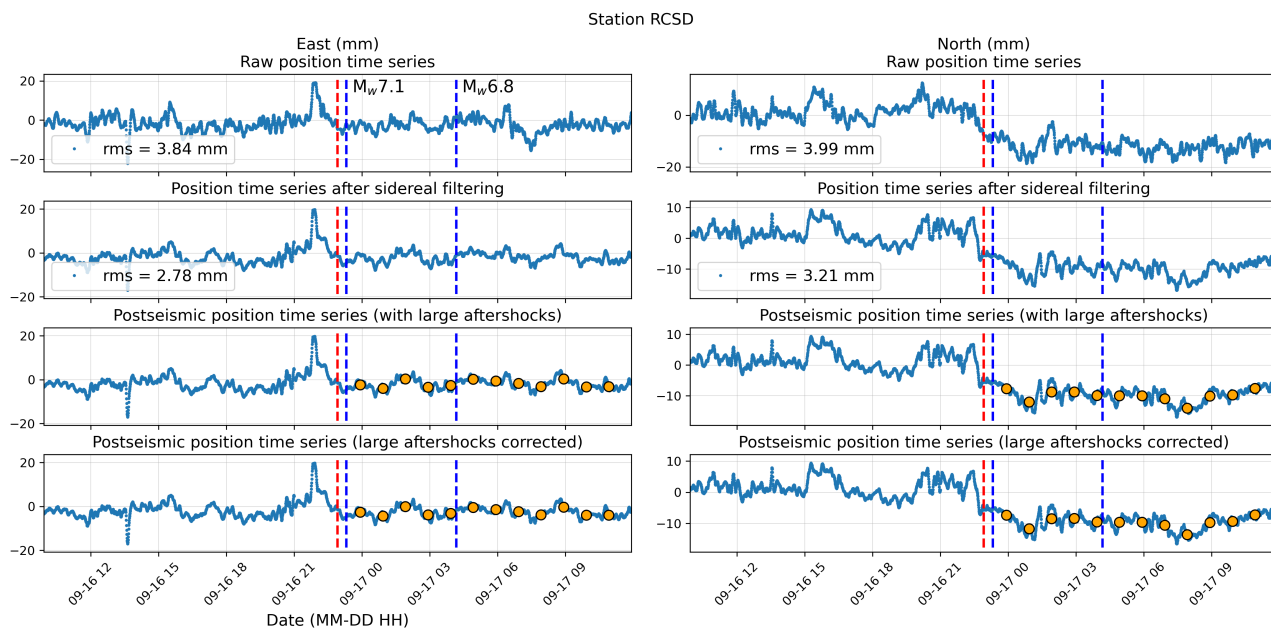


Figure S2.15. Same as Figure 2 in the main text.

S3 Choice of the smoothing parameter

As mentioned in the main text, the cost function has the following form:

$$\varepsilon = \frac{1}{N} \frac{\sum_{i=1}^N ((o_i - c_i)/e_i)^2}{\sum_{i=1}^N o_i^2} + \omega \Lambda \quad (1)$$

- 25 where N is the number of observations (2 horizontal components \times number of receivers), e is the error associated to the observation, Λ is the Laplacian of the slip distribution and ω is the weight given to the Laplacian. In order to choose ω we tested different values ranging from 1.0×10^{-6} and up to 1.0×10^6 . We use the L curve criterion to select the optimum value (Hansen, 1992). Based on the results shown in Figure S3.1 we choose 0.1 as the optimum value (red dot on Figure S3.1).

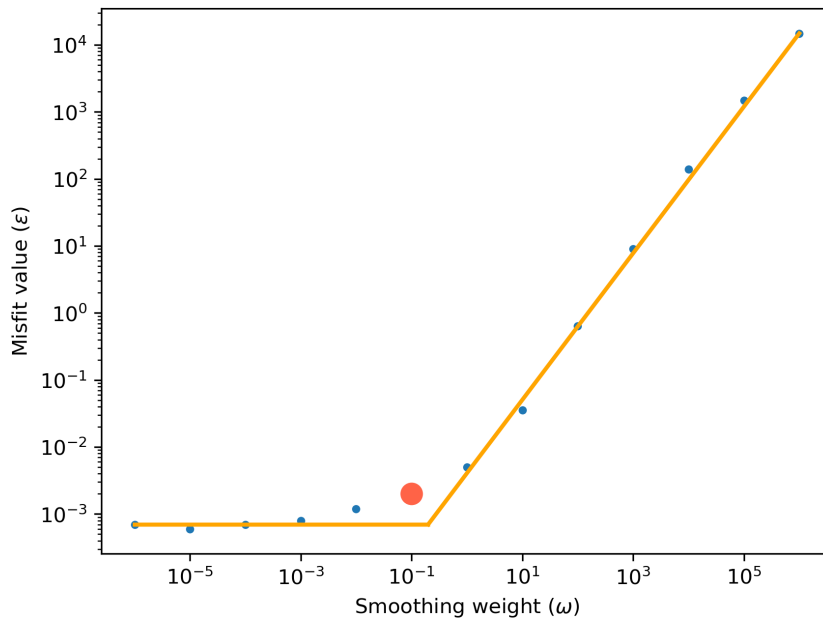


Figure S3.1. Evolution of the misfit as a function of the weight given to the Laplacian smoothing Λ (blue dots). The large red dot shows the selected value based on the L-curve criterion (Hansen, 1992). The orange line outlines the trend.

S4 Summary of the results from the inversions.

- 30 In the following figures (Figure S4.1 to S4.15), we show a comparison between the observed position time series (blue) and the position time series calculated from the average post-seismic slip model (orange). Figure S4.16 shows a comparison between the observed and the calculated surface displacements in a map view at each time step. Finally, Figure S4.17 shows the rake angle for the average post-seismic slip model.

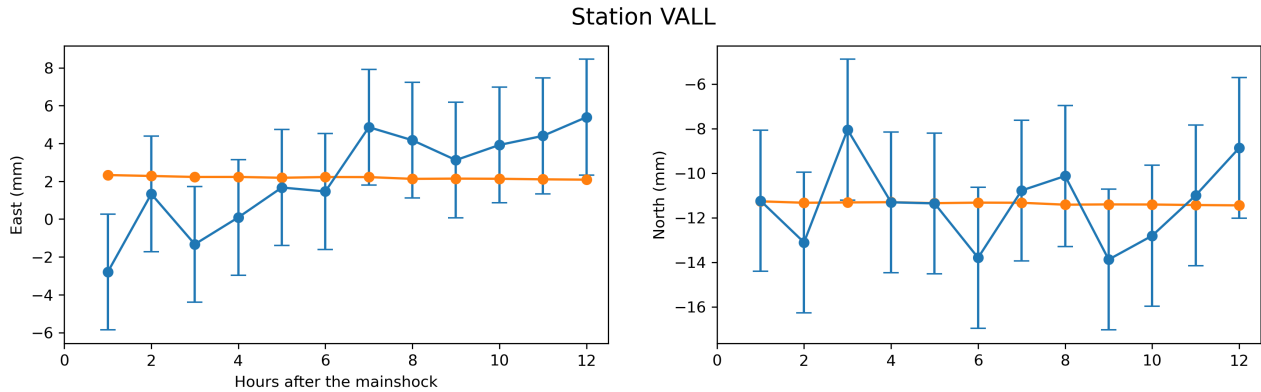


Figure S4.1. Blue dots show the observations along with their uncertainties, and the orange dots show the prediction from the average post-seismic slip model.

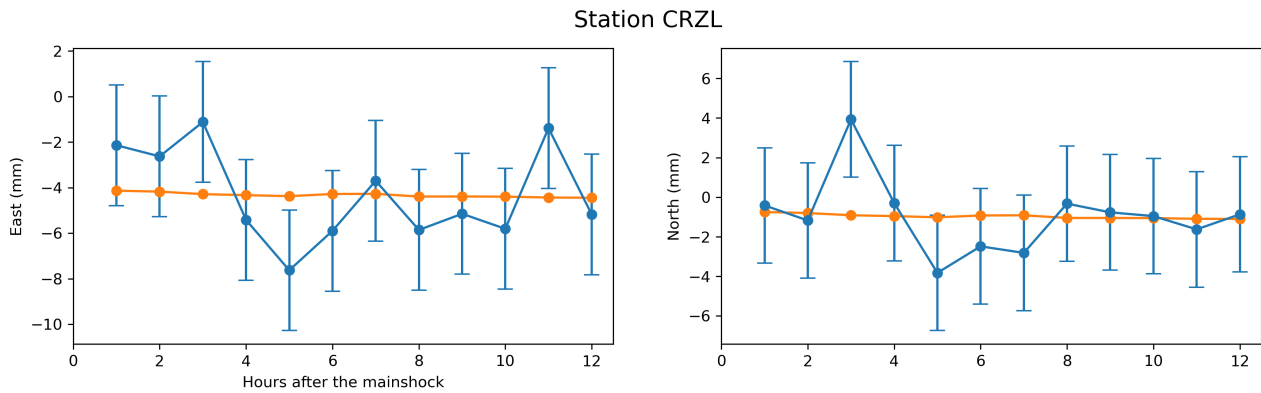


Figure S4.2. Blue dots show the observations along with their uncertainties, and the orange dots show the prediction from the average post-seismic slip model.

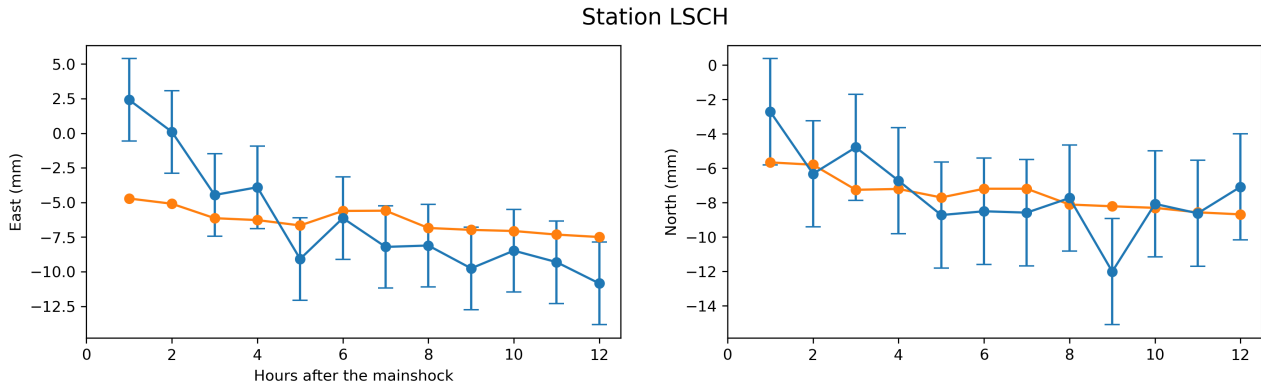


Figure S4.3. Blue dots show the observations along with their uncertainties, and the orange dots show the prediction from the average post-seismic slip model.

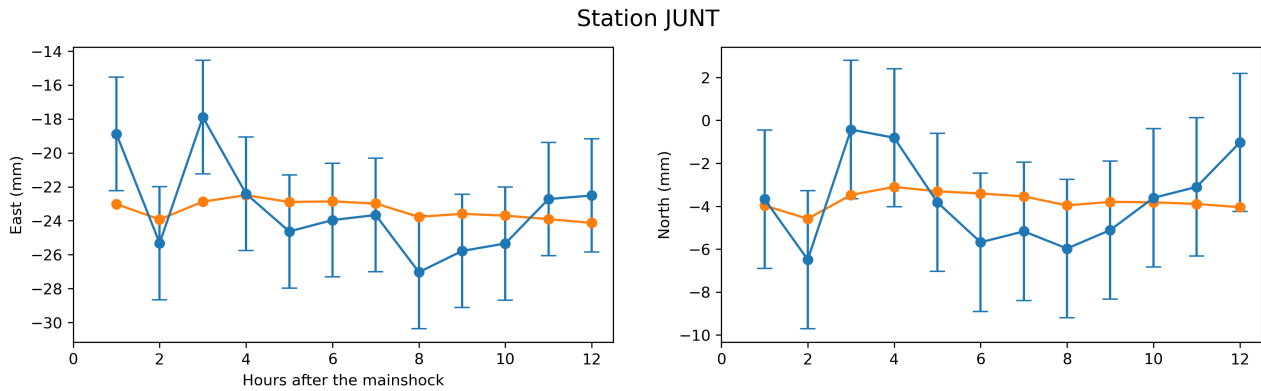


Figure S4.4. Blue dots show the observations along with their uncertainties, and the orange dots show the prediction from the average post-seismic slip model.

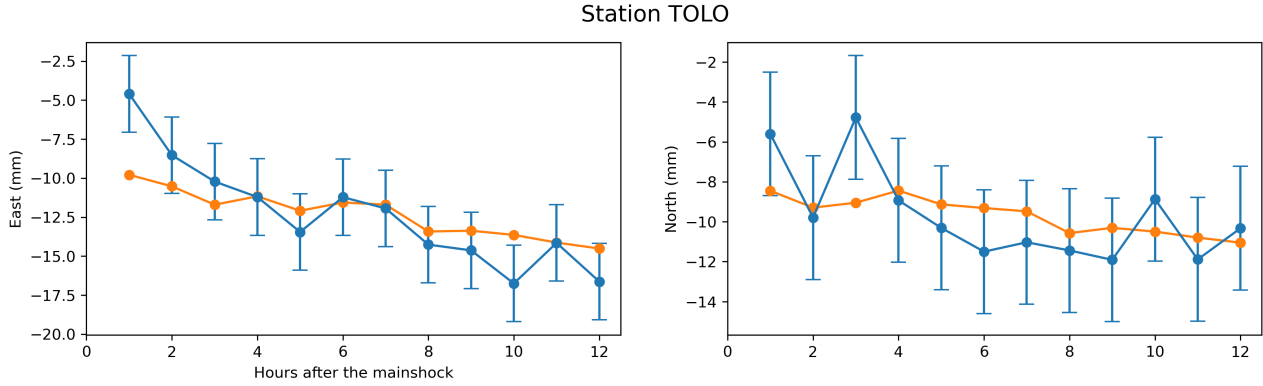


Figure S4.5. Blue dots show the observations along with their uncertainties, and the orange dots show the prediction from the average post-seismic slip model.

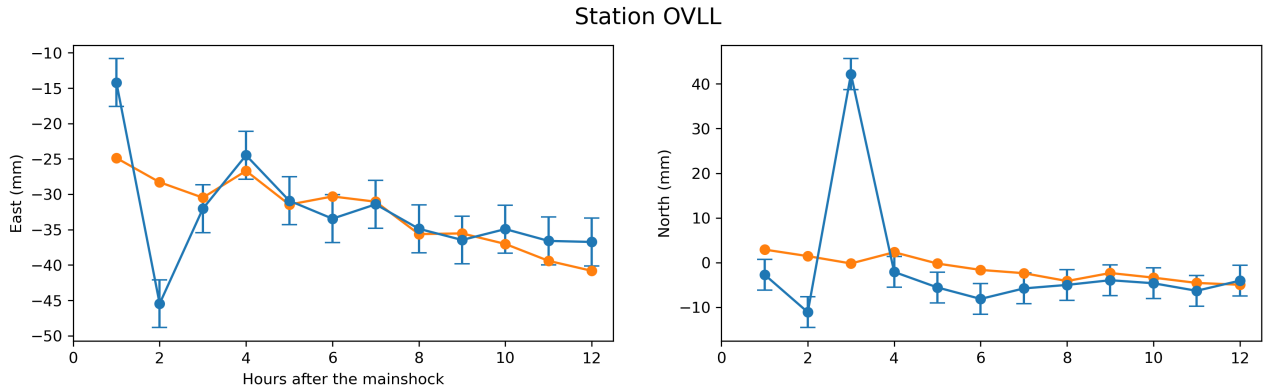


Figure S4.6. Blue dots show the observations along with their uncertainties, and the orange dots show the prediction from the average post-seismic slip model. As mentioned in the main text, hours 2 and 3 at this station are disregarded during the inversion because the high-rate position time series show strong spurious signal that are not of tectonic origin, which consequently affect the averaging.

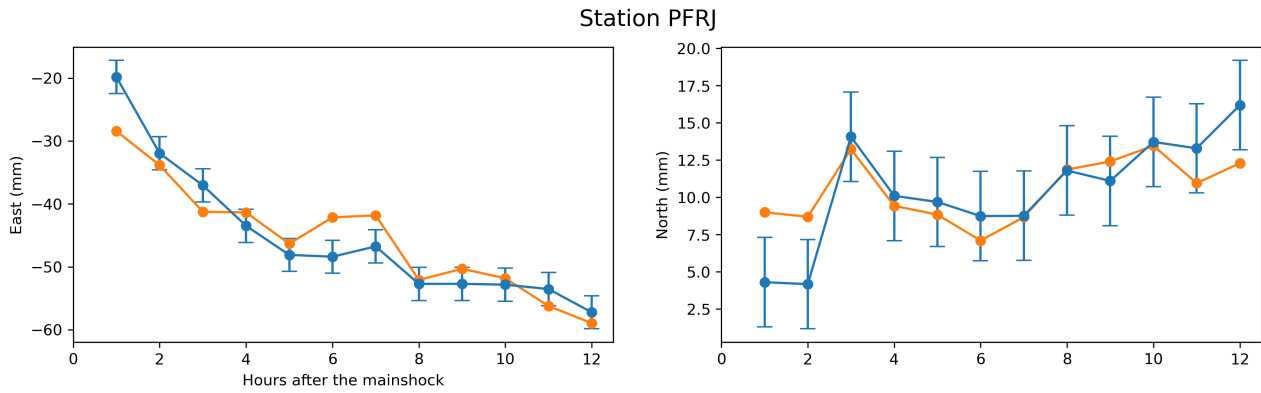


Figure S4.7. Blue dots show the observations along with their uncertainties, and the orange dots show the prediction from the average post-seismic slip model.

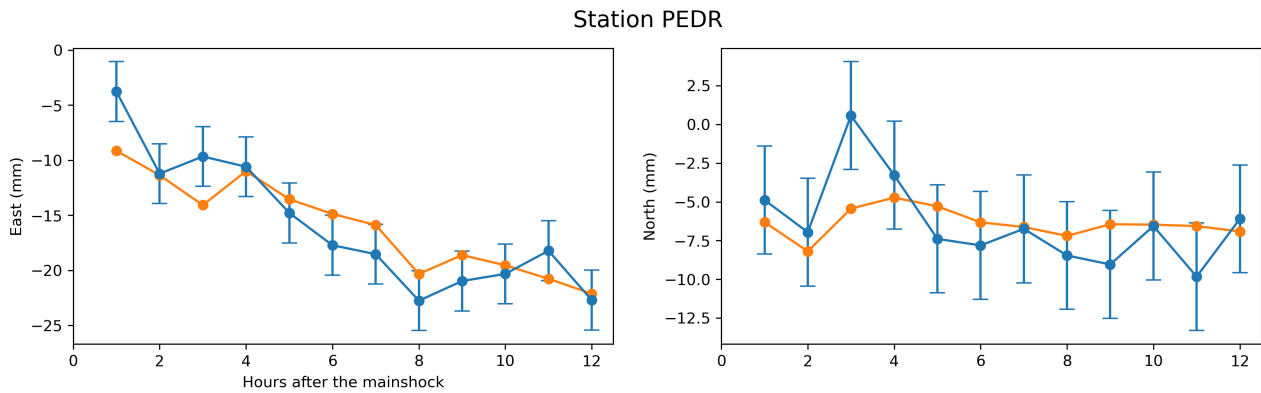


Figure S4.8. Blue dots show the observations along with their uncertainties, and the orange dots show the prediction from the average post-seismic slip model. Blue dots show the observations along with their uncertainties, and the orange dots show the prediction from the average post-seismic slip model.

Station CMBA

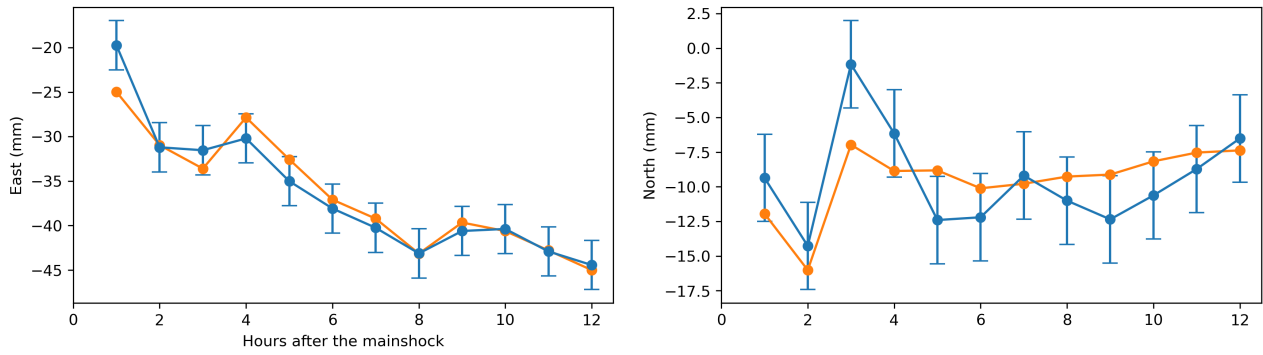


Figure S4.9. Blue dots show the observations along with their uncertainties, and the orange dots show the prediction from the average post-seismic slip model.

Station CNBA

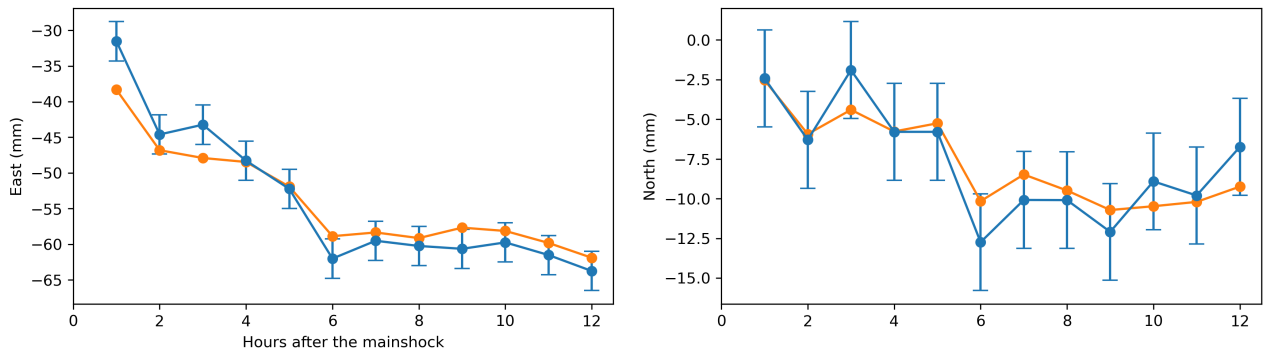


Figure S4.10. Blue dots show the observations along with their uncertainties, and the orange dots show the prediction from the average post-seismic slip model.

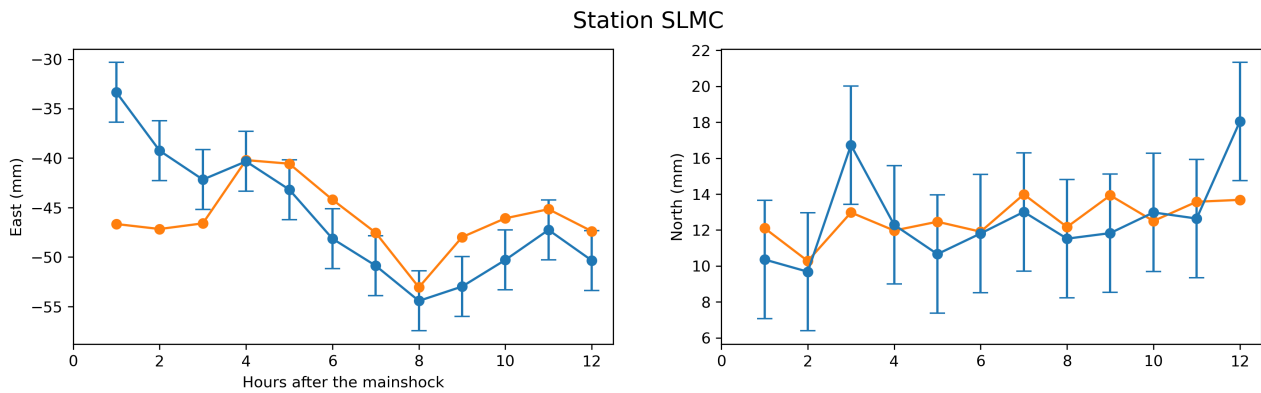


Figure S4.11. Blue dots show the observations along with their uncertainties, and the orange dots show the prediction from the average post-seismic slip model.

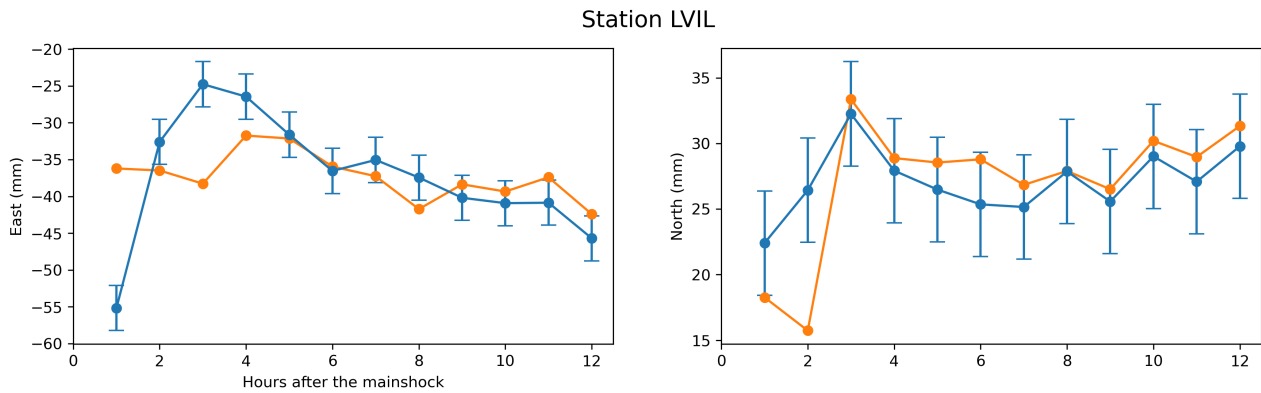


Figure S4.12. Blue dots show the observations along with their uncertainties, and the orange dots show the prediction from the average post-seismic slip model. As mentioned in the main text, the first 2 hours at this station are disregarded during the inversion because the high-rate position time series show strong spurious signal that are not of tectonic origin, which consequently affect the averaging.

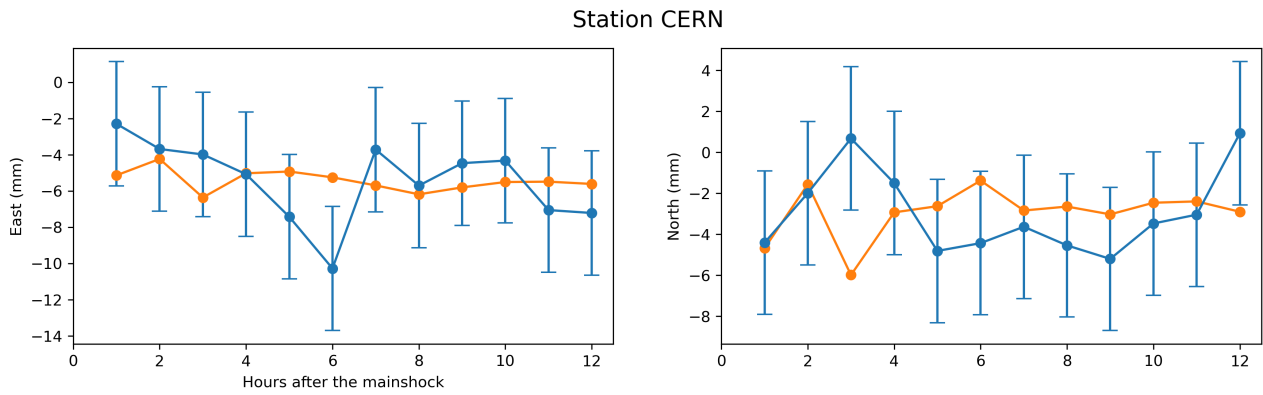


Figure S4.13. Blue dots show the observations along with their uncertainties, and the orange dots show the prediction from the average post-seismic slip model.

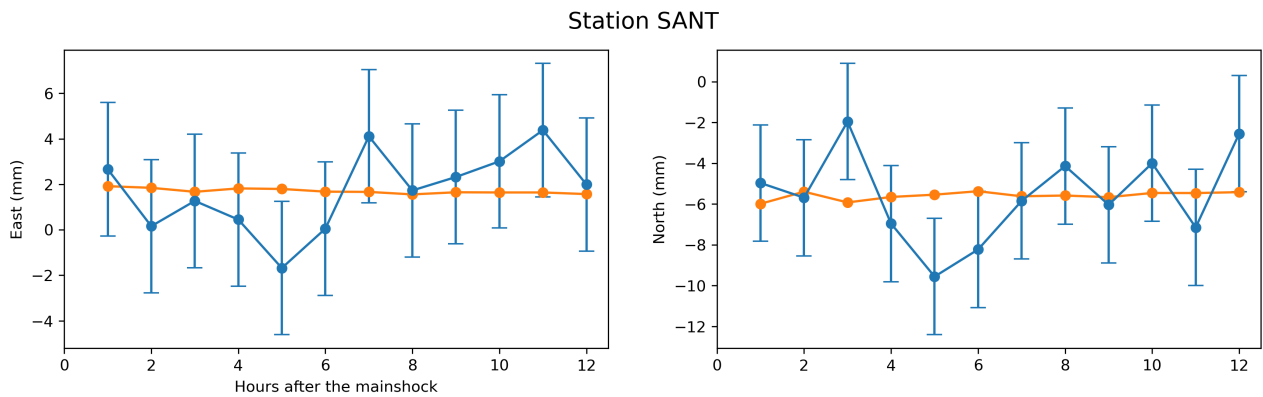


Figure S4.14. Blue dots show the observations along with their uncertainties, and the orange dots show the prediction from the average post-seismic slip model.

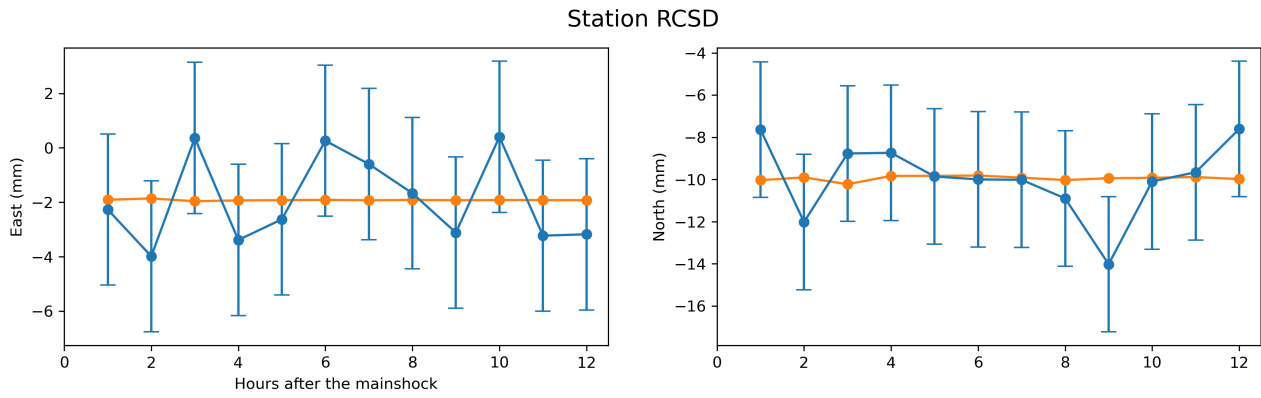


Figure S4.15. Blue dots show the observations along with their uncertainties, and the orange dots show the prediction from the average post-seismic slip model.

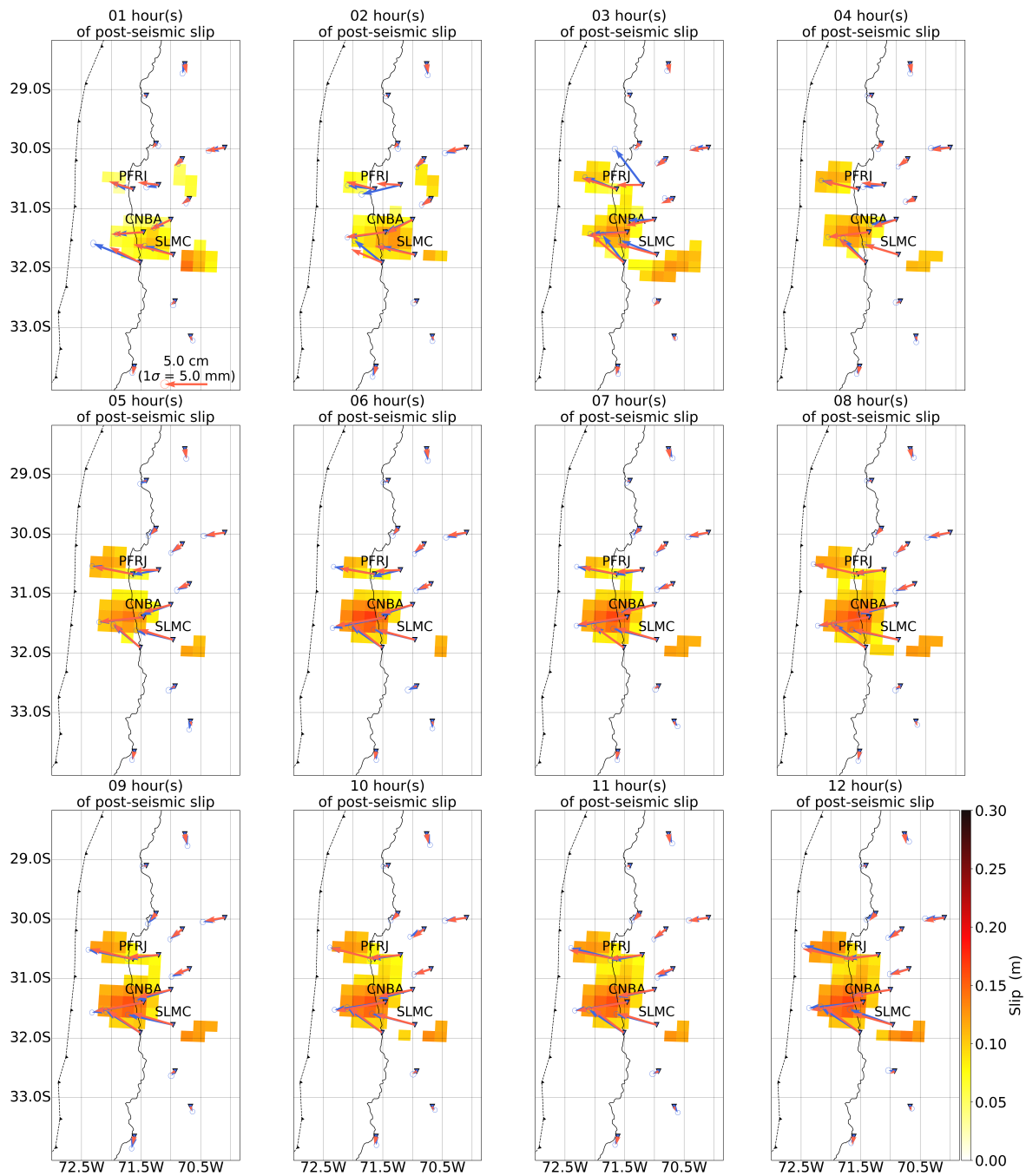


Figure S4.16. Map showing the observed horizontal displacements (blue arrows) and the predicted horizontal displacements (red arrows) for the average post-seismic slip model.

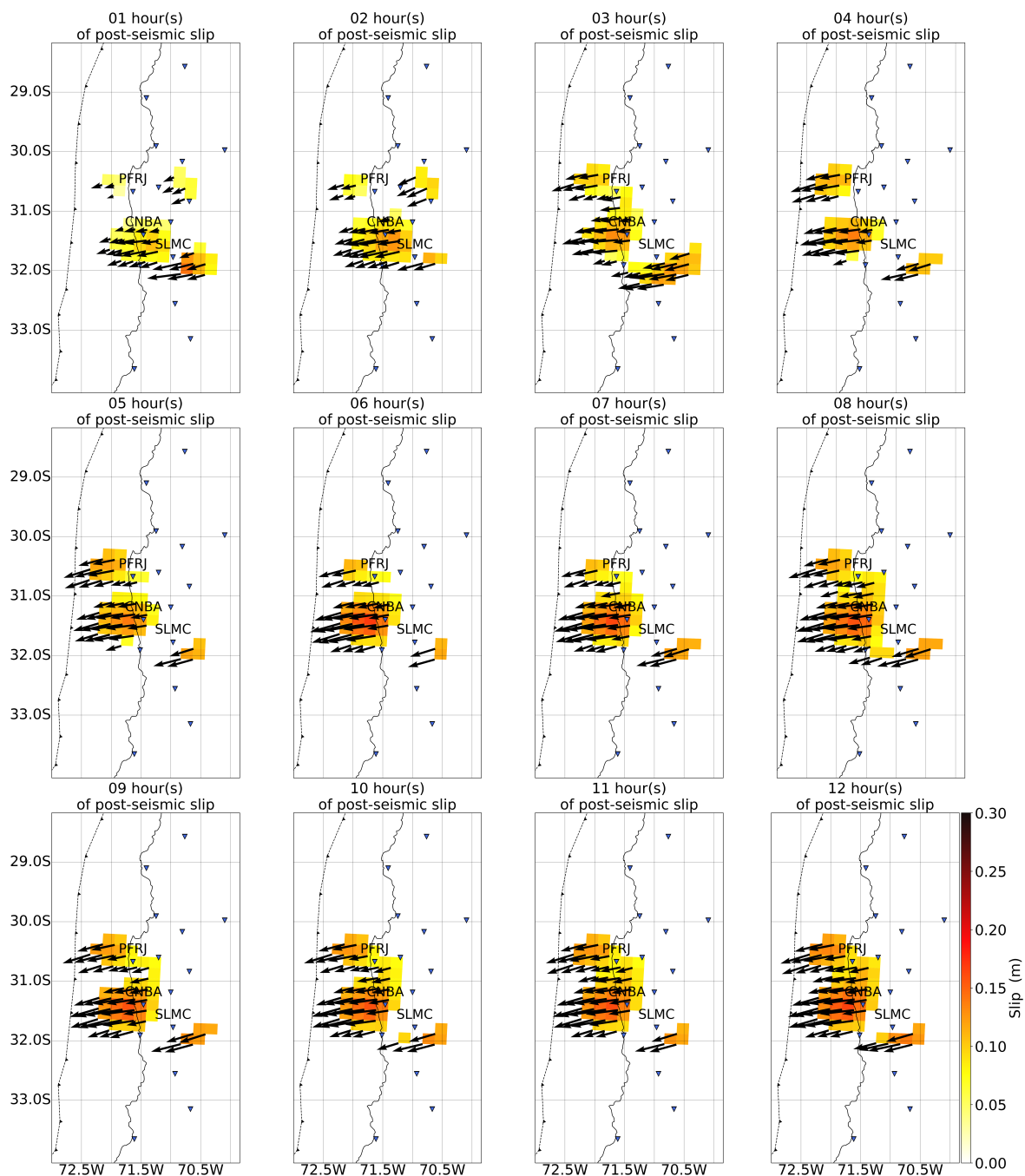


Figure S4.17. Map showing the obtained rake angle for the average post-seismic slip model. During the inversion the rake angle is allowed to vary by $\pm 15^\circ$ about the rake angle of the mainshock given by the GCMT catalog (i.e., 109°). The length of the arrows reflect the slip amplitude.

S5 Sensitivity analysis

35 In order to check the reliability of the afterslip models that we have obtained, we perform various sensitivity tests. First, we start by doing a resolution analysis. We compute the resolution matrix following Tarantola and Valette (1982):

$$R = C_m G^t (G C_m G + C_d)^{-1} G \quad (2)$$

where G are the Green's functions, C_d the data covariance matrix and C_m the model covariance matrix. The model covariance matrix is calculated using the ensemble of models that we have obtained from our inversion procedure after weighting each model by the inverse of the misfit. We first look at the diagonal elements of the resolution matrix (Figure S5.1a). This indicates if slip of a given subfault is correctly mapped to that particular subfault (Radiguet et al., 2011). We find the resolution appears rather low everywhere. This, is expected as the number of model parameters is large compared to the number of observation, an issue that is accounted for by introducing smoothing during the inversion. But the low resolution does not mean that slip cannot be recovered. Instead, it rather means that slip might not be recovered at the correct location (Page et al., 2009). Therefore, we investigate the strength of subfault-correlation by looking at the off-diagonal structure of R . In particular, we look at it for a subfault located at the center of the northern patch (Figure S5.1b) as well as for a subfault located at the center of the southern patch (Figure S5.1c). For both location, we find that slip is smeared out over a certain area, but it is not smeared much beyond the delineated areas that we use for the discussion in the main text. But, we notice that for the southern patch (Figure S5.1c), it is possible that some slip gets misallocated in a region that is south of station SLMC, which will be discussed later. However, overall, we find that the slip that we image in the northern and southern patches are likely to be relatively well located.

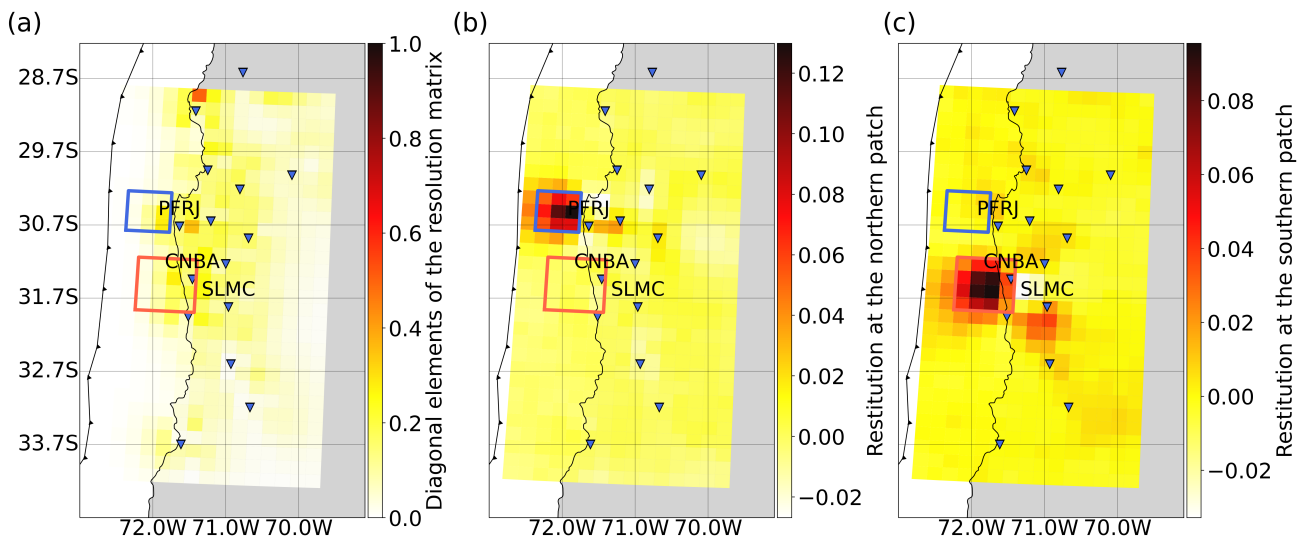


Figure S5.1. (a) Map of the diagonal elements of the resolution matrix. (b) Map showing the off-diagonal elements of the resolution matrix for a subfault that is located inside the northern patch discussed in the main text and highlighted by the blue square. (c) Map showing the off-diagonal elements of the resolution matrix for a subfault that is located inside the southern patch discussed in the main text and highlighted by the red square.

Another way that we can assess the reliability of the afterslip model is by looking at the relative standard deviation (RSD) and that is the ratio between the standard deviation and the mean model (Figure S5.2). We find that in the northern and the southern patch, the RSD is rather low suggesting that slip in these regions is well constrained, except for the first couple of hours in the northern patch. We also find that the deep region of afterslip located south-east of Salamanca (station SLMC) always has a large RSD. Thus, this region remains on the map simply because its amplitude is just a little bit higher than the

standard deviation. That might suggest that this patch is rather unreliable. Based on the previous observation we made from looking at the resolution matrix, it is possible that this patch represents slip from the southern patch that is mis-located here because of a smearing effect.

60 Still, we further investigate the reliability of this deep patch of slip by looking at the impact it makes on surface displacements. Figure S5.3 and Figure S5.4 show the surface displacements induced by this patch at the surface on the north and east components, respectively. We only display regions where the amplitude of the surface displacements is larger than the lowest noise level among all the stations (i.e., 2.45 mm).

65 On the north component, we find that CERN and SLMC are potentially affected by the deep patch of afterslip, which contributes at most to -5.4 mm and 3.6 mm at these stations, respectively. For SLMC, we find that the contribution of that deep patch is very small compared to the observed displacement (see Figure S4.11), suggesting a rather negligible impact on the misfit. This is not so much the case for CERN (see Figure S4.13). However, the amplitude of the observed displacements on the north component at this station barely exceeds the noise level.

70 On the east component, we find that LVIL and SLMC are potentially affected. This time, it contributes at most to -6.0 mm and -4.2 mm at these stations, respectively. However, for both stations, we find that this contribution is quite small with respect to the observed surface displacements (see Figure S4.12 and Figure S4.11). Therefore, it is once again likely that this deep afterslip patch has a negligible impact on the misfit.

75 Two additional qualitative arguments can also be proposed as to why this patch is unreliable. First, Figure 3 in the main text shows that this patch does not exhibit a steady spatio-temporal evolution unlike all other regions of afterslip. That might reflect the fact that this patch helps to fit spurious signals in the time series rather than the manifestation of a transient phenomenon. Second, when we use the position time-series corrected from the 2 largest aftershocks (Figure 7 in the main text), we observe that the patch disappears almost completely. In our opinion, these arguments support even further the fact that this patch is likely to be unreliable rather than tectonically induced.

Therefore, based on these different arguments, we argue that this patch is not reliable, which is why we do not include it in the discussion in the main text.

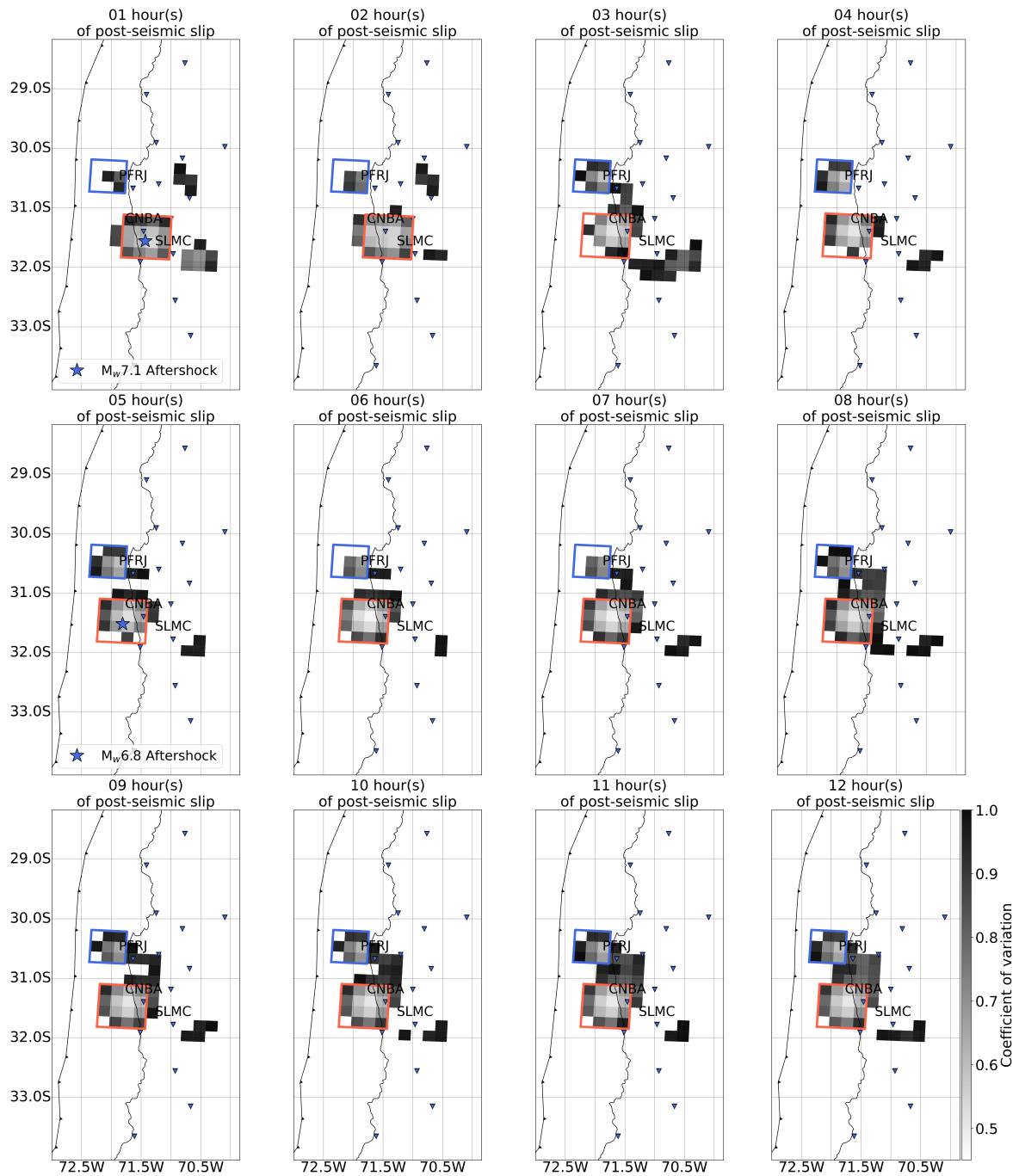


Figure S5.2. Maps of the coefficient of variation otherwise called the relative standard deviation (RSD) and that is the ratio between the standard deviation and the mean model.

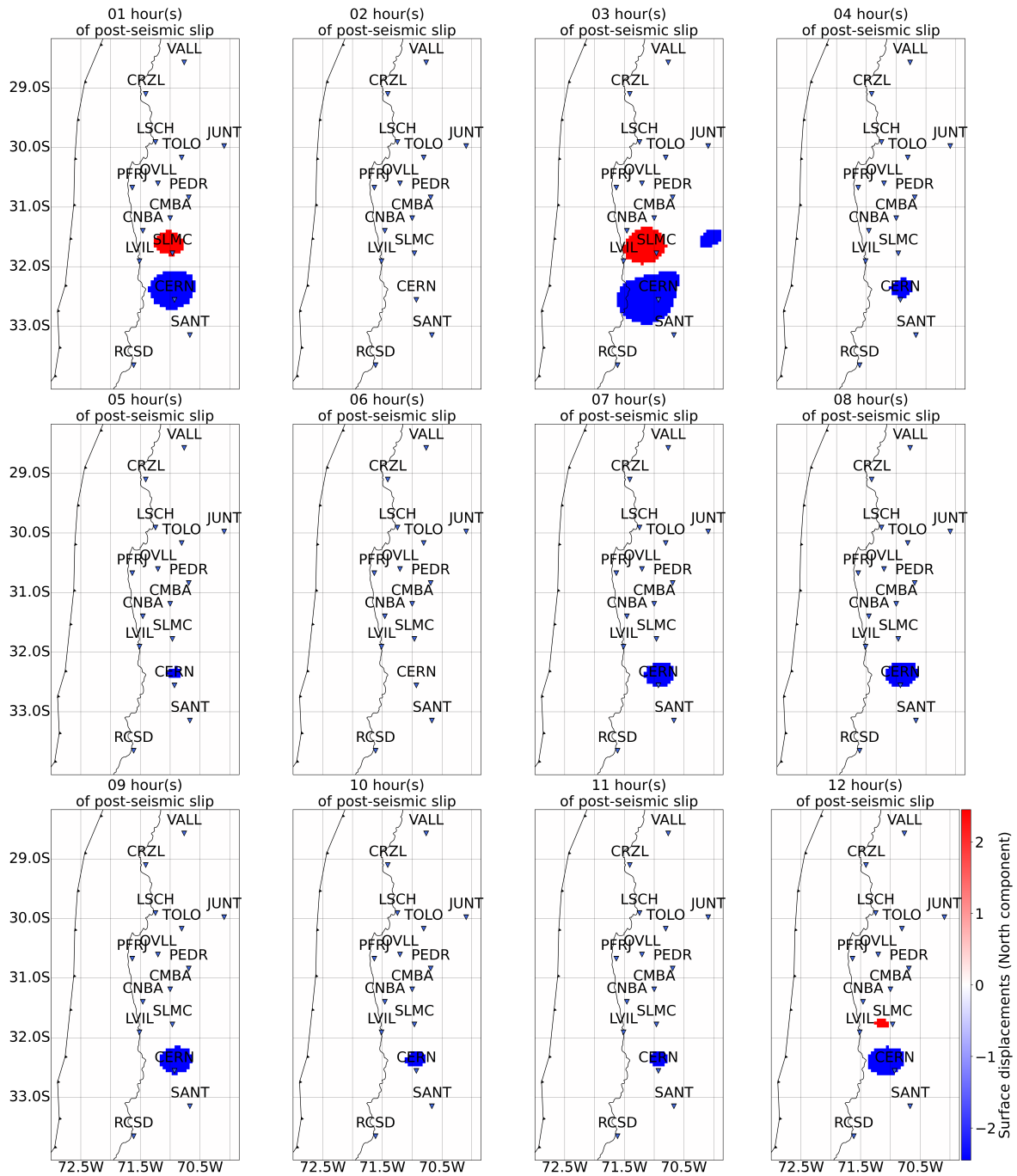


Figure S5.3. Surface displacements induced by the deep afterslip patch on the north component. The maps only show regions where the amplitude of the generated signal is larger than the lowest noise level among all stations (i.e., 2.45 mm)

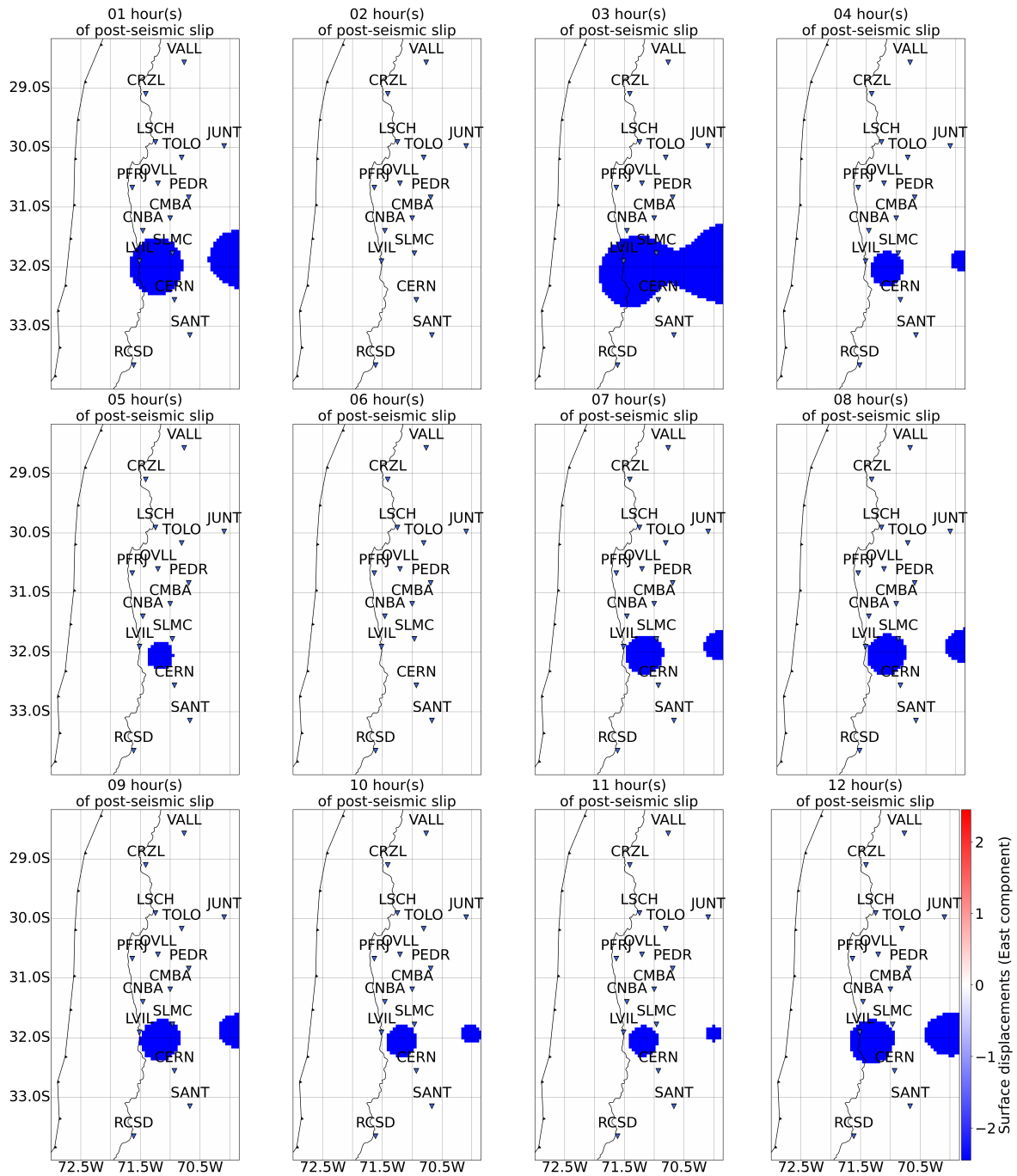


Figure S5.4. Surface displacements induced by the deep afterslip patch on the east component. The maps only show regions where the amplitude of the generated signal is larger than the lowest noise level among all stations (i.e., 2.45 mm)

80 S6 Comparison between the post-seismic slip model and various co-seismic slip models

Here, we compare the very-early post-seismic slip distribution after 12 hours with a non-exhaustive list of co-seismic rupture model from the literature (Figure S6.1). The model by Okuwaki et al. (2016) is the only one that is obtained using seismological data only (teleaseismic waveforms). Thus, it is not at all contaminated by very-early afterslip. However, because only far-field data are used, it is likely that this model does not have the best resolution compared to the others. Melgar et al. (2016) uses the most complete dataset by including seismological data, tsunami data, high-rate GNSS data and InSAR data. Some contamination from very-early afterslip can be expected in the InSAR data since the tracks have been acquired 1 and 3 days after the mainshock. But, despite the fact InSAR data is used, most of the data are not contaminated by very-early post-seismic slip. Therefore, it is unlikely that the slip distribution contains a strong signature from the very-early post-seismic slip. This is why it has been chosen for the discussion in the main text. The model by Tillmann et al. (2015) is also obtained from a combination of seismological data and geodetic data (static offsets from GNSS data). Depending on the weighting adopted for each dataset, this model can be more or less affected by very-early post-seismic slip occurring during the first 12 hours. The remaining models presented are obtained using geodetic data only and are thus likely to be more or less contaminated by very-early afterslip. The model by (Shrivastava et al., 2016) is obtained using static co-seismic offsets measured from daily GNSS data. This is also the case for the model by (Ruiz et al., 2016). Then, the model by (Barnhart et al., 2016) is obtained by adding InSAR data. Finally, the co-seismic slip model obtained by Klein et al. (2017) comes from a combination of InSAR data, static co-seismic offsets from daily GNSS data and strict co-seismic offsets measured from high-rate GNSS data. Note that for almost all models, the 1-m slip contour is displayed on the figure (2-m for the model by Klein et al. (2017)).

We also compare our post-seismic slip model with the co-seismic slip model that we have obtained using the co-seismic static offsets determined from our position time series (see Table 3). We follow the same inversion procedure as described in the main text. The only differences are that the range explored for the slip amplitude goes from 0 to 10m, and the weight given to the Laplacian smoothing has been adapted to a value of 0.01 based on the same approach as given in Section S3. We compare the co-seismic slip model, calculated as the average of the ensemble of models that we have obtained from our inversion procedure, with the post-seismic slip model (Figure S6.2). We find that the core region of maximum slip amplitude (black dashed line in Figure S6.2) lies in between the two main areas of post-seismic slip. More generally, the 1-m co-seismic slip contour (pink dashed line in Figure S6.2) is in agreement with the different models from the literature (Figure S6.1).

In addition, we provide some indications about the reliability of the co-seismic model. The comparison between the observed and predicted horizontal offsets at the surface are in good agreement (see Figure S6.3a). We also show the restitution calculated from the resolution matrix for the sub-fault that exhibits the largest slip amplitude (Figure S6.3b). We note that for computing the resolution matrix, the model covariance matrix has been re-calculated using the ensemble of co-seismic models that we have obtained from our inversion procedure to account for the updated weight given to the Laplacian smoothing (see Section S5 for more details on the computation of the resolution matrix). It shows that the region of large co-seismic slip (hereafter called core region) is to the first order well located. But, we also find some leakage of slip north-east of the core region (hereafter called NE region). This means either that the peak slip is overestimated (i.e., slip in the core region being wrongly attributed here instead of the NE region), or that the peak slip is underestimated (i.e., slip in the NE region rather corresponds to slip in the core region).

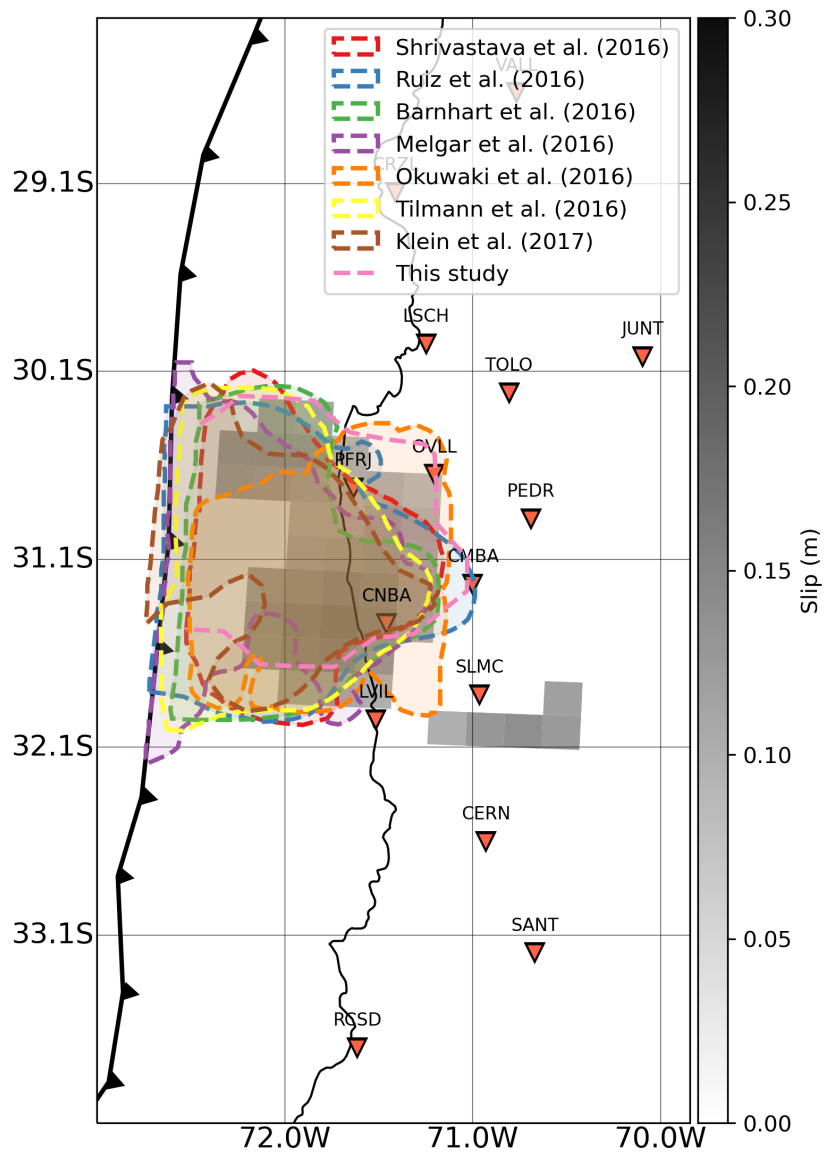


Figure S6.1. Comparison between our post-seismic slip model (grey colors) with different co-seismic slip models from the literature (dashed line). The dashed lines shows the 1-m slip contour except for the model by Klein et al. (2017), which shows the 2-m slip contour.

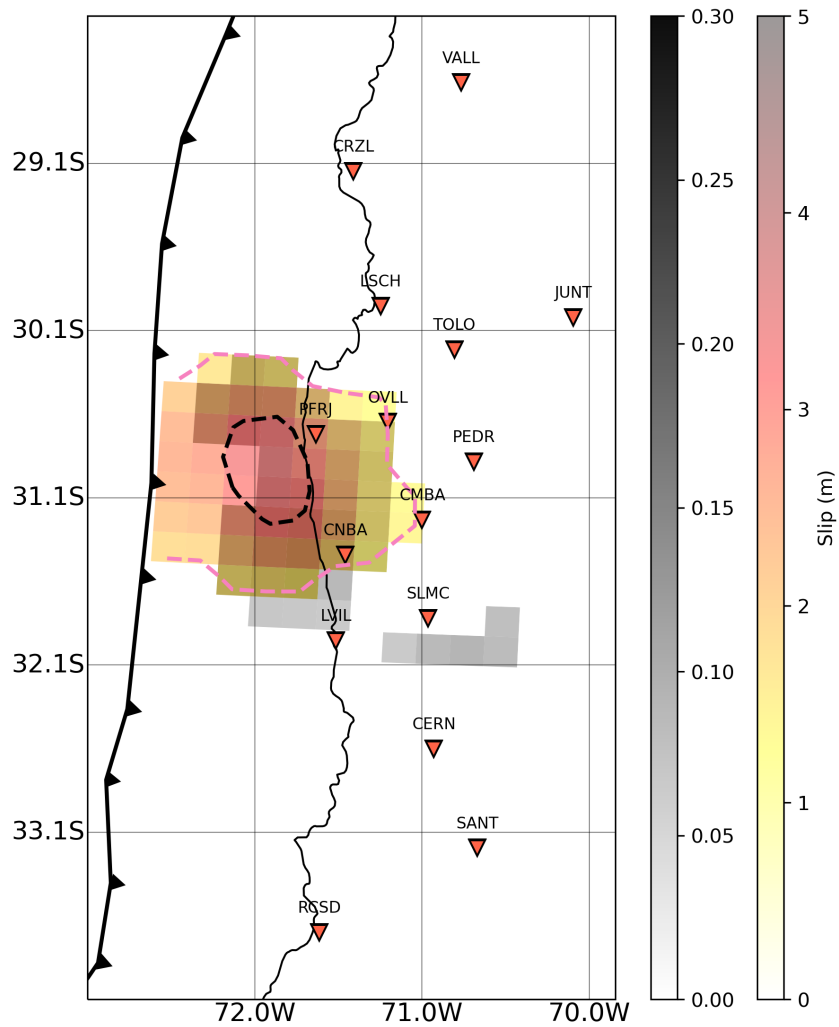


Figure S6.2. Comparison between our post-seismic slip model (grey colors) with our co-seismic slip model (yellow to grey colors). We also show the 1-m slip contour of the co-seismic slip model with the pink dashed line. The 3-m slip contour is also shown with the black dashed line

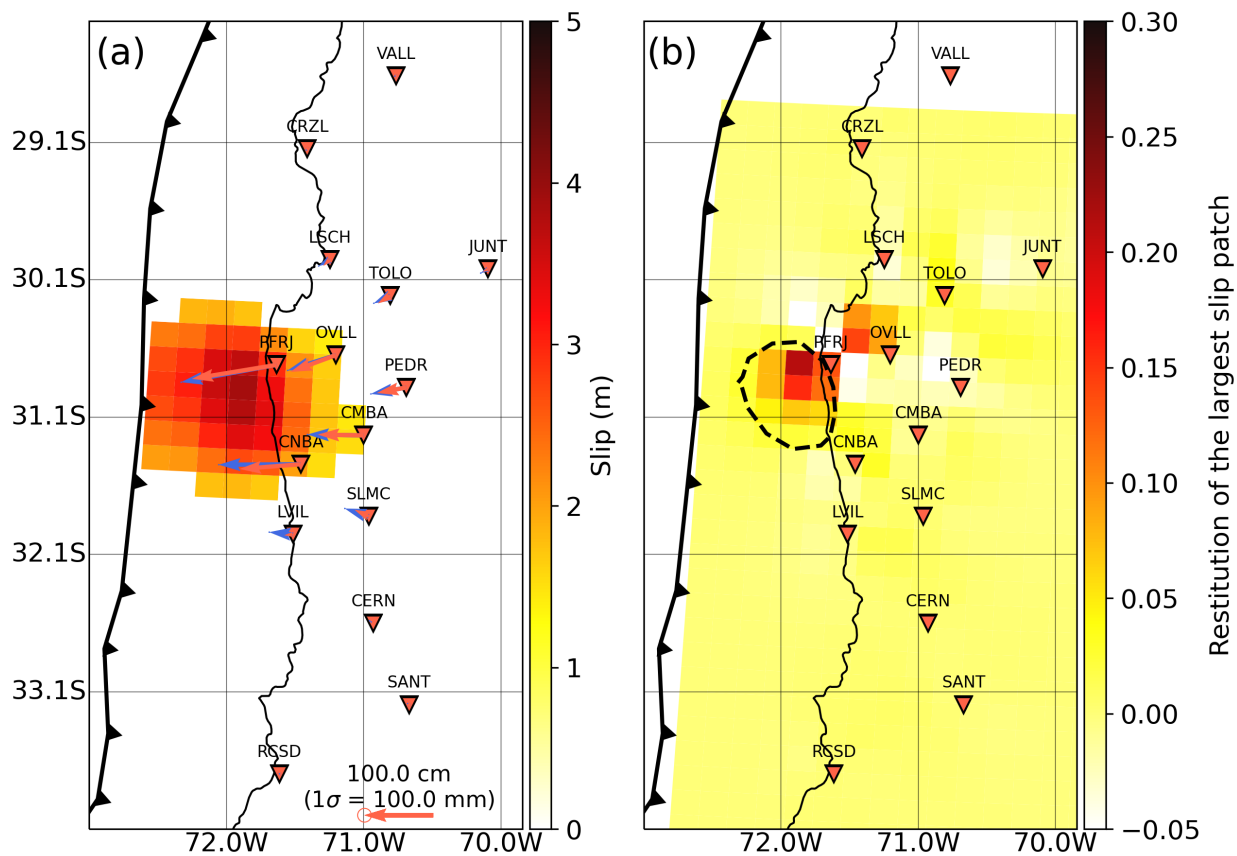


Figure S6.3. (a) Comparison between the observed horizontal co-seismic offsets (blue arrows) with the prediction made using the co-seismic slip model (red arrows). The average co-seismic slip distribution is shown in the background of the map. (b) Restitution computed from the resolution matrix for the sub-fault that exhibits the largest slip amplitude. The 3-m slip contour is shown with the black dashed line.

S7 Comparison between very early post-seismic slip and very early aftershocks using Frank et al. (2017) catalog

In order to ensure that our conclusions are not strongly dependent on the chosen catalog, we also make a comparison between our post-seismic slip models and the catalog of aftershocks obtained from template-matching techniques by Frank et al. (2017). As shown by Figure S7.1, we observe an nearly identical pattern as what we observe using the catalog from Huang et al. (2017).

120 Over the first 2 hours, most of the seismic activity occurs south of the rupture area, just as does the post-seismic slip. To the north, very little activity is seen during these first 2 hours but it then progressively intensifies just like the post-seismic slip. After the first 12 hours of the post-seismic phase, we see a pattern where post-seismic slip and aftershocks strongly overlap, both surrounding the co-seismic rupture area.

125 Finally, we also compare the afterslip and aftershock temporal evolution using the aftershocks catalog from Frank et al. (2017) to ensure our conclusions about their relationship are not dependent of the catalog. We find the same relationship between the cumulative afterslip and the cumulative number of aftershocks in the north patch (Figure S7.2).

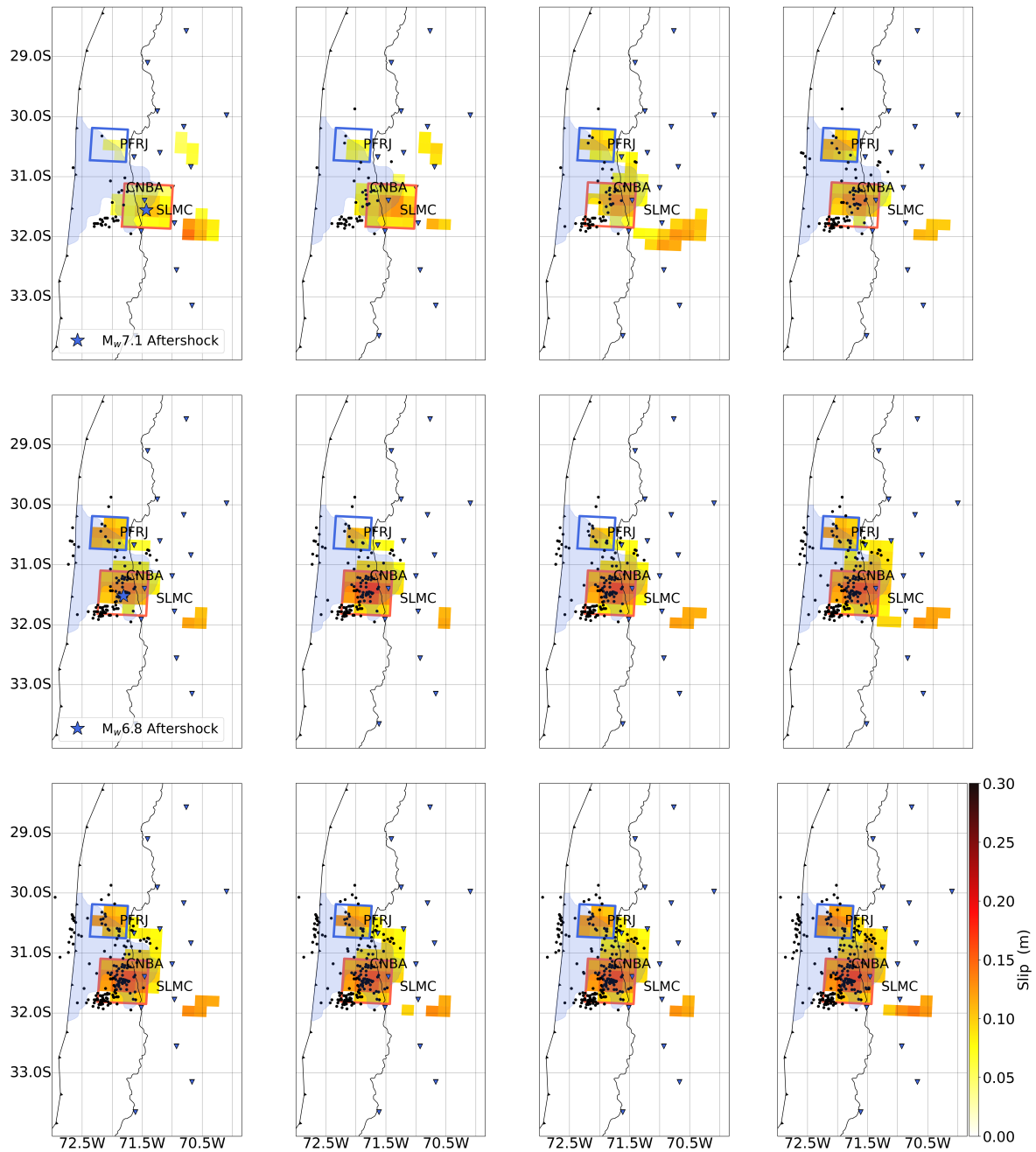


Figure S7.1. Same as Figure 5 in the main text, except that the aftershock catalog is from Frank et al. (2017).

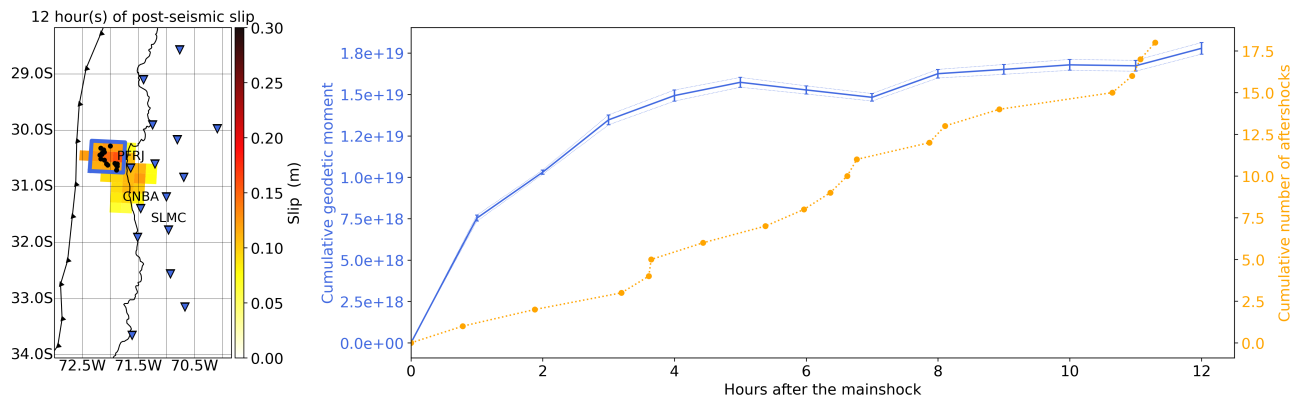


Figure S7.2. Same as Figure 8 in the main text, except that the aftershock catalog is from Frank et al. (2017).

References

- Barnhart, W. D., Murray, J. R., Biggs, R. W., Gomez, F., Miles, C. P. J., Svarc, J., Riquelme, S., and Stressler, B. J.: Coseismic slip and early afterslip of the 2015 Illapel, Chile, earthquake: Implications for frictional heterogeneity and coastal uplift, *J. Geophys. Res. Solid Earth*, 121, 6172–6191, <https://doi.org/10.1002/2016JB013124>, 2016.
- 130 Frank, W. B., Poli, P., and Perfettini, H.: Mapping the rheology of central Chile subduction zone with aftershocks, *Geophys. Res. Lett.*, 44, 5374–5382, <https://doi.org/10.1002/2016GL072288>, 2017.
- Hansen, C.: Analysis of discrete ill-posed problems by means of the L-curve, *SIAM Rev.*, 34, 561–580, <https://doi.org/10.1137/1034115>, 1992.
- 135 Huang, H., Xu, W., Meng, L., B urgmann, R., and Baez, J. C.: Early aftershocks and afterslip surrounding the 2015 Mw 8.4 Illapel rupture, *Earth Planet. Sci. Lett.*, 457, 282–291, <https://doi.org/10.1016/j.epsl.2016.09.055>, 2017.
- Klein, E., Vigny, C., Fleitout, L., Grandin, R., Jolivet, R., Rivera, E., and Metois, M.: A comprehensive analysis of the Illapel 2015 Mw 8.3 earthquake from GPS and InSAR data, *Earth Planet. Sci. Lett.*, 469, 123–134, <https://doi.org/10.1016/j.epsl.2017.04.010>, 2017.
- Melgar, D., Fan, W., Riquelme, S., Geng, J., Liang, C., Fuentes, M., Vargas, G., Allen, R. M., Shearer, P. M., and Fielding, E.: Slip
140 segmentation and slow rupture to the trench during the 2015 Mw 8.3 Illapel, Chile, earthquake, *Geophys. Res. Lett.*, 43, 961–966, <https://doi.org/10.1002/2015GL067369>, 2016.
- Okuwaki, R., Yagi, Y., Aranguiz, R., Gonzalez, R., and Gonzalez, G.: Rupture process during the 2015 Illapel, Chile earthquake: Zigzag-along-dip rupture episodes, *Pure Appl. Geophys.*, 173, 1011–1020, <https://doi.org/10.1007/s00024-016-1271-6>, 2016.
- Page, M., Custodio, S., Archuleta, R., and Carlson, J.: Constraining earthquake source inversions with GPS Data 1: resolution based removal of artifacts, *J. Geophys. Res.*, 114, B01 314, <https://doi.org/10.1029/2007JB00544>, 2009.
- 145 Radiguet, M., Cotton, F., Vergnolle, M., Campillo, M., Valette, B., Kostoglodov, V., and Cotte, N.: Spatial and temporal evolution of a long term slow slip event: the 2006 Guerrero Slow Slip Event, *Geophys. J. Int.*, 184, 816–828, <https://doi.org/10.1111/j.1365-246X.2010.04866.x>, 2011.
- Ruiz, S., Klein, E., del Campo, F., Rivera, E., Poli, P., Metois, M., Vigny, C., Baez, J. C., Vargas, G., Leyton, F., Madariaga, R.,
150 and Fleitout, L.: The Seismic Sequence of the 16 September 2015 Mw 8.3 Illapel, Chile, Earthquake, *Seism. Res. Lett.*, 87, <https://doi.org/10.1785/0220150281>, 2016.
- Shrivastava, M. N., Gonzalez, G., Moreno, M., Chlieh, M., Salazar, P., Reddy, C. D., Baez, J. C., nez, G. Y., Gonzalez, J., and de la Llera, J. C.: Coseismic slip and afterslip of the 2015 Mw 8.3 Illapel (Chile) earthquake determined from continuous GPS data, *Geophys. Res. Lett.*, 43, 10 710–10 719, <https://doi.org/10.1002/2016GL070684>, 2016.
- 155 Tarantola, A. and Valette, B.: Generalized non-linear inverse problems solved using the least square criterion, *Rev. Geophys. Space Phys.*, 20, 219–232, <https://doi.org/10.1029/RG020i002p00219>, 1982.
- Tillmann, F., Zhang, Y., Moreno, M., Saul, J., Eckelmann, F., Palo, M., Deng, Z., Babeyko, A., Chen, K., Baez, J. C., Schurr, B., Wang, R., and Dahm, T.: The 2015 Illapel earthquake, central Chile: A type case for a characteristic earthquake ?, *Geophys. Res. Lett.*, 43, 574–583, <https://doi.org/10.1002/2015GL066963>, 2015.
- 160 Twardzik, C., Vergnolle, M., Sladen, A., and Avallone, A.: Unravelling the contribution of early postseismic deformation using sub-daily GNSS positioning, *Sci. Rep.*, 9, <https://doi.org/10.1038/s41598-019-39038-z>, 2019.